A&A, 707, A70 (2026)
https://doi.org/10.1051/0004-6361/202557970

Astronomy & Astrophysics

Constraining the size, shape, and albedo of the large trans-Neptunian object (28978) Ixion with multi-chord stellar occultations

Y. Kilic[1,2,⋆], F. Braga-Ribas[3,4,2], C. L. Pereira[5,4], J. L. Ortiz[1], B. Sicardy[6], P. Santos-Sanz[1], O. Erece[7,8], J. L. Rizos[1], J. M. Gómez-Limón[1], G. Margoti[5,4], D. Souami[2,9], B. Morgado[10], A. Gomes-Junior[11,4,12], L. M. Catani[10,1], J. Desmars[13,6], M. Kretlow[1,14], F. Rommel[15], R. Duffard[1], A. Alvarez-Candal[1], J. I. B. Camargo[5,4], M. Kaplan[16], N. Morales[1], D. Herald[17], M. Assafin[10,4], G. Benedetti-Rossi[2,5,4], R. Sfair[12,18,2], R. Savalle[19], J. Arcas-Silva[5], L. Bernasconi[20], T. Blank[21], M. Bonavita[22], N. Carlson[21], B. Christophe[23], C. A. Colesanti[24,†], M. Collins[25], G. Columba[26], R. Dunford[21], D. W. Dunham[27], J. Dunham[21], M. Emilio[5,28], W. G. Ferrante[3], T. George[21†], W. Hanna[21], G. Isopi[29,30,31,32], R. Jones[21], D. A. Kenyon[33], S. Kerr[17], V. Kouprianov[34], P. D. Maley[21,35], F. Mallia[30], J. Mattei[36], M. Meunier[37], T. Napoleao[24], V. F. Peixoto[10,4], J. Pollock[38,†], C. Snodgrass[22], A. Stechina[39], W. Thomas[21], R. Venable[21], G. R. Viscome[21,40], A. Zapparata[30], J. Bardecker[21], N. Castro[41], C. Cebral[42], A. Chapman[43], C. Gao[44], K. Green[44,45], A. Guimaraes[12], C. Jacques[46,47], E. Jehin[48], M. Konishi[42], R. Leiva[1], L. Liberato[49], C. Magliano[42], L. A. Mammana[50,51], M. Melita[52], V. Moura[12], Y. Olivera-Cuello[42], L. Peiro[53], J. Spagnotto[54], P. C. Stuart[21], L. Vanzi[41], A. Wilberger[55], and M. Malacarne[56]

(Affiliations can be found after the references)

Received 4 November 2025 / Accepted 12 January 2026

ABSTRACT

Context. Trans-Neptunian objects (TNOs) are among the most primitive remnants of the early Solar System. Determining their sizes, shapes, albedos, and surface properties is essential for understanding their origin and evolution. Stellar occultations provide highly accurate size and shape information for TNOs, while photometry constrains their albedo and surface colours. (28978) Ixion is one of the largest TNOs and a prominent Plutino, making it a key target for comparative studies.

Aims. The aim of this work is to constrain Ixion's projected size, shape, absolute magnitude, geometric albedo, and surface colours, and to search for evidence of an atmosphere or circum-object material.

Methods. We conducted a series of campaigns targeting stellar occultations by Ixion between 2020 and 2023 as part of the Lucky Star collaboration, gathering 51 observations from eight events, including 30 positive detections. Five multi-chord events were used for a global limb fit, enabling an accurate reconstruction of Ixion's projected shape. Calibrated photometric data, including new and archival measurements, were analysed to derive its absolute magnitude, phase-curve parameters, and broadband colours.

Results. The multi-chord occultations reveal a slightly elongated limb that is well represented by a single projected ellipse with semi-axes $a = 363.42^{+3.53}_{-3.85}$ km and $b = 333.98^{+7.07}_{-4.96}$ km, yielding $R_{\rm equiv} = 348.39^{+5.37}_{-4.43}$ km ($D_{\rm equiv} = 696.78^{+10.75}_{-8.87}$ km), and an apparent oblateness $\epsilon' = 0.081^{+0.004}_{-0.010}$. The geometry is consistent with a moderately flattened, nearly spheroidal body that may show slight departures from axial symmetry. The typical radial residuals (∼10 km) support a largely stable shape across the observed epochs, with modest epoch-dependent variations. The phase-curve fit gives $H_V = 3.845 \pm 0.006$, $\beta = 0.1301 \pm 0.0078$ mag deg^{-1}, and $p_V = 0.106^{+0.003}_{-0.003}$. Multi-band photometry yields $B - V = 1.06 \pm 0.03$, $V - R = 0.61 \pm 0.02$, and $R - I = 0.54 \pm 0.03$, which is consistent with moderately red TNO surfaces. No atmosphere or circum-object material was detected down to our sensitivity limits. The best-sampled event (13 October 2020) also allowed us to measure the angular diameter of the occulted star Gaia DR3 4056440205544338944, $\theta_\star = 0.670 \pm 0.010$ mas, which corresponds to $R_\star = 128 \pm 10\,R_\odot$ at the *Gaia* distance.

Key words. methods: data analysis – methods: observational – astrometry – occultations – planets and satellites: general – Kuiper belt objects: individual: (28978) Ixion

1. Introduction

The stellar occultation technique is one of the most precise Earth-based methods for determining the physical properties of trans-Neptunian objects (TNOs). Since the first successful observation of a stellar occultation by a TNO other than Pluto or Charon, in 2009 (Elliot et al. 2010), this technique has provided highly accurate size measurements with kilometre-level precision and constraints on atmospheric properties down to nanobar levels (e.g. Sicardy et al. 2024; Braga-Ribas et al. 2013), and has enabled the discovery and characterisation of ring systems around objects such as Chariklo, Chiron, Haumea, and Quaoar (Braga-Ribas et al. 2014; Ortiz et al. 2015, 2017; Sickafoose et al. 2020; Ortiz et al. 2023; Morgado et al. 2023; Pereira et al. 2023, 2025; Santos-Sanz et al. 2025). Additionally, stellar occultations have revealed topographic features on TNO surfaces, offering insights into surface irregularities and compositions (Dias-Oliveira et al. 2017; Rommel et al. 2023).

⋆ Corresponding author: yucel@yucelkilic.com
† Deceased.

Table 1. Equivalent diameters of (28978) Ixion from various studies.

Year	Diameter (km)	Method	Reference
2002	1055 ± 165	Radiometry	Bertoldi et al. (2002)
2003	<804	Radiometry	Altenhoff et al. (2004)
2004	<822	Optical + thermal	Grundy et al. (2005)
2005	475 ± 75	Thermal	Stansberry et al. (2005)
2007	480^{+152}_{-136}	Thermal + radiometry	Cruikshank et al. (2007)
2008	650^{+260}_{-220}	Thermal (Spitzer)	Stansberry et al. (2008)
2008	590 ± 190	Thermal	Brown (2008)
2013	~549	Thermal (Herschel–Spitzer)	Mommert (2013)
2013	617^{+19}_{-20}	Thermal (Herschel–Spitzer)	Lellouch et al. (2013)
2021	>709.6 ± 0.2	Single chord stellar occ.	Levine et al. (2021)

Observations of moons, such as Vanth (Orcus/1) and Weywot (Quaoar/1) (Sickafoose et al. 2019; Braga-Ribas et al. 2025), further emphasise the technique's power in the study of outer Solar System objects. Further occultation studies have also constrained the sizes of smaller TNO satellites, such as Hi'iaka (Fernández-Valenzuela et al. 2025), Namaka (Rommel et al. 2025b), Huya's moon (Rommel et al. 2025a), 2014WC$_{510}$ (Leiva et al. 2020), and 2000YW$_{134}$ (Vara-Lubiano et al. 2023), as well as the shapes of Centaurs, such as 2002 GZ$_{32}$ (Santos-Sanz et al. 2020), Chiron (Braga-Ribas et al. 2023), Echeclus (Pereira et al. 2024), and Bienor (Rizos et al. 2024), with the shape and spatial orientation of the Centaur Chariklo being a notable example (Leiva et al. 2017; Morgado et al. 2021).

Trans-Neptunian objects are icy remnants from the early Solar System beyond Neptune. Their study provides valuable insights into the primordial conditions of Solar System formation and evolution (Lykawka & Mukai 2008; Morbidelli et al. 2008). Among them is (28978) Ixion, a large Plutino orbiting the Sun in a 3:2 resonance with Neptune. With an estimated diameter in the ~700 km range (see Table 1) and moderately red surface properties, Ixion ranks among the brightest Plutinos and represents a key target for detailed investigation.

To date, around 259 stellar occultations involving 57 TNOs and 14 Centaurs have been observed, but only 41 have yielded multi-chord observations[1]. Multi-chord data are essential for accurately determining the shapes, sizes, and densities of these distant bodies. Among these, Ixion stands out due to its unique orbital configuration and physical properties. Ixion was discovered in May 2001 at the Cerro Tololo Inter-American Observatory during the Deep Ecliptic Survey (Minor Planet Center 2002). As part of the group of Plutinos in a 3:2 mean-motion resonance with Neptune, Ixion is a relevant target for studying Neptune's migration history and its influence on the dynamical evolution of the Kuiper Belt. Such resonance-locked configurations are understood in the framework of the resonance capture mechanism proposed by Malhotra (1995).

Ixion's orbital parameters closely resemble those of Pluto, with a semi-major axis a = 39.35 au, an eccentricity e = 0.244, and an inclination i = 19.67°[2]. However, Ixion's slightly higher inclination and distinct surface characteristics make it an intriguing object of study.

The latest equivalent diameter, reported as 709.6 ± 0.2 km from a nearly single-chord stellar occultation (Levine et al. 2021), was derived under the assumption of a circular limb. As acknowledged in that study, the very small formal uncertainty naturally follows from this modelling choice, given that the event geometry provides only limited information on the limb shape. The multi-chord events analysed here therefore complement that result by providing direct constraints on the limb geometry.

Understanding Ixion's physical structure and potential for hydrostatic equilibrium provides critical insights into the processes governing the evolution of such objects (Grundy et al. 2019). The absolute magnitude (H_V) of Ixion has been measured as 3.774 ± 0.021 mag (Alvarez-Candal et al. 2016), and its geometric albedo (p_V) is calculated to be 0.108 ± 0.002 (Verbiscer et al. 2022). Photometric measurements indicate a $B-V$ colour index of 1.03 ± 0.03 mag and a $V-R$ colour index of 0.61 ± 0.03 mag, suggesting a moderately red surface (Doressoundiram et al. 2007).

Ixion's rotation period has not been conclusively determined, and studies on this subject have provided varying results. The first attempt to measure Ixion's rotation period was conducted by Ortiz et al. (2003), but no periodicity was identified in the light curve, which had an amplitude of <0.15 mag. A subsequent study by Sheppard & Jewitt (2003) also failed to detect any significant variability, setting an upper limit of 0.05 mag for the light curve amplitude. This value is notably lower than the amplitude reported by Ortiz et al. (2003), highlighting its importance. The first successful determination of Ixion's rotation period was achieved in 2010 using the 3.58 m New Technology Telescope (NTT) at the European Southern Observatory (ESO). Rousselot & Petit (2010) derived a period of 15.9 ± 0.5 h assuming a single-peaked light curve with an amplitude of 0.06 ± 0.03 mag. Based on more recent observations by Galiazzo et al. (2016) at the Las Campanas Observatory, using the 1 m Swope Telescope, Ixion's rotation period was estimated to be 12.4 ± 0.3 h. This determination is one of several published period estimates, and – like the others – should be regarded as a plausible solution rather than a definitive constraint on Ixion's rotation state. However, Ixion moves in a crowded stellar field near the Galactic plane, and its photometric measurements are frequently affected by contamination from faint background stars, making the determination of a precise rotational period particularly challenging.

Ixion's surface composition has also been investigated using near-infrared spectroscopy, which suggests a mix of dark organic materials, amorphous carbon, and possibly traces of water ice and silicates (Boehnhardt et al. 2004; Barkume et al. 2008). Although no satellite has been observed around Ixion, its surface properties are similar to those of Quaoar (which has a satellite called Weywot), another large TNO known for its water ice and tholins.

This article is organised as follows. Section 2 explains our strategy for predicting the stellar occultations analysed in this work. Section 3 describes the observations obtained from different sites and instruments, and presents the resulting positive chords. Section 4 details the analysis of the light curves, which led to constraints on the stellar radius of one of the occulted stars as well as Ixion's size, shape, and physical parameters (absolute magnitude, phase curve, albedo, and colours). Finally, Sect. 5 discusses the implications of our results and summarises the main conclusions.

2. Predictions

The remarkable astrometric precision achieved by the *Gaia* data releases (Gaia Collaboration 2016a,b, 2018, 2023) has markedly improved the reliability of occultation predictions by providing stellar coordinates at the sub-milliarcsecond level

[1] Based on Braga-Ribas (priv. comm.) and the `Occultation Portal` database: https://occultationportal.org

[2] JPL Small-Body Database: https://ssd.jpl.nasa.gov/

Table 2. J2000 star coordinates, proper motions, parallaxes, magnitudes, and NIMA solutions used for each prediction.

Date	Designation	RA (ICRS)	errRA (mas)	Dec (ICRS)	errDec (mas)	pmRA (mas yr^{-1})	pmDec (mas yr^{-1})	Plx (mas)	G (mag)	NIMA Version
28 Jul. 2023	4049162851669604096	$18^h11^m3.2654^s$	0.025	–31°15′22.477″	0.020	1.748	–5.399	0.108	14.53	NIMAv12
30 Jun. 2022	4049905056379149824	$18^h06^m53.6148^s$	0.033	–30°46′56.476″	0.029	–4.367	–8.163	0.111	15.00	NIMAv11
2 Jun. 2022	4049248613603980416	$18^h09^m36.9353^s$	0.030	–30°43′37.051″	0.025	0.067	–6.964	0.166	15.19	NIMAv11
17 Aug. 2021	4056220440657653248	$17^h56^m18.8133^s$	0.168	–30°17′43.765″	0.131	–5.521	–3.726	–0.074	16.93	NIMAv11
20 May 2021	4050180170543871104	$18^h04^m5.2362^s$	0.025	–30°13′44.615″	0.021	–2.538	–5.993	0.284	14.18	NIMAv11
28 Apr. 2021	4050000576486883840	$18^h05^m34.6814^s$	0.034	–30°09′09.703″	0.030	–3.730	–7.404	0.101	14.84	NIMAv11
13 Oct. 2020	4056440205544338944	$17^h50^m20.3595^s$	0.040	–29°43′33.087″	0.031	0.235	0.273	0.565	10.31	NIMAv10
17 Aug. 2020	4056438835548480896	$17^h49^m53.5830^s$	0.023	–29°48′12.589″	0.018	1.007	–1.704	0.293	14.52	NIMAv8

Notes. RA and Dec are barycentric coordinates propagated to the occultation epoch. Errors are standard errors in RA (corrected by $\cos\delta$) and Dec. Proper motions are also adjusted. Plx: absolute parallax. G: *Gaia* G-band magnitude. NIMA: numerical integration of the motion of an asteroid solution used for each event prediction.

(Rommel et al. 2020). Under these conditions, the dominant source of uncertainty arises from the TNO's ephemeris.

To address this, we generated updated orbital solutions for Ixion employing the NIMA algorithm (Desmars et al. 2015)[3], progressively incorporating new astrometric observations and successive *Gaia* catalogues (DR2, EDR3, and DR3) across multiple epochs. The iterative refinement of the orbit, culminating in the NIMAv12 solution, enabled predictions with temporal and spatial accuracy sufficient to design and execute observation campaigns with a high probability of success. In addition, astrometric offsets obtained close to the occultation dates (e.g. from the Observatorio de Sierra Nevada, the Calar Alto Observatory, and the Liverpool Telescope) were incorporated to further improve the predictions.

The predicted mid-times and reference star information for each event are summarised in Table 2, including the numerical integration of the motion of an asteroid (NIMA) solution applied in each case. The observed occultation chords derived from these predictions are displayed in Fig. C.1, allowing a direct comparison between the predicted shadow paths and the actual detections.

3. Observations

Stellar occultation campaigns for (28978) Ixion were conducted between 2020 and 2023 as part of the Lucky Star collaboration[4]. These campaigns resulted in varying numbers of positive detections, ranging from one to eight chords per event, contributing to a comprehensive multi-chord analysis of Ixion. Observational data, including site status and event details, were collected and managed using the `Occultation Portal`[5], as described in Kilic et al. (2022). A summary of these campaigns, including the number of chords, detection outcomes, and the main geometric and observational parameters of each occultation (geocentric distance, apparent sky-plane velocity, stellar angular diameter, and characteristic spatial sampling), is presented in Table 3.

Across all campaigns, most observers conducted their measurements in 'clear' mode (no optical filter) to maximise the signal-to-noise ratio. Weather conditions were generally favourable at the majority of sites, yielding high-quality light curves throughout the 2020–2023 observing period. Detailed information for each event – including observing configurations (telescope aperture, camera type, cadence), filter usage, exposure times, and site-specific weather reports – is provided in Table D.1.

3.1. 17 August 2020 occultation

On 17 August 2020, the occultation of the star Gaia DR3 4056438835548480896 (G = 14.52; see Table 2) was recorded from three stations in the United States (Chester, Naperville, and Lake Placid). The predicted mid-time was 01:42:15 UT, the corresponding shadow path is shown in Fig. C.1a, and the event parameters are summarised in Table 3.

Each site reported a positive detection of the occultation. Video and imaging systems with precise timing capabilities were utilised to determine ingress and egress times accurately. The Chester station utilised a WAT-910HX video camera synchronised via Network Time Protocol (NTP), while Naperville and Lake Placid operated QHY174-GPS cameras, providing direct GPS timestamps. Exposure times ranged between 0.3 s and 5 s, depending on the system configuration and observing conditions. All observers used a luminance (L) filter during the acquisition. Image sequences were initiated approximately 5 minutes before the predicted event time and continued for at least 5 minutes afterwards. As seen at Lake Placid (Fig. E.0a), the disappearance was visually noticed just before the recording was initiated. Observers also reported meteorological and seeing conditions to support the assessment of the light-curve quality (see Table D.1).

3.2. 13 October 2020 occultation

On 13 October 2020, the occultation was recorded from ten sites across the United States (see Table D.1). The target star was Gaia DR3 4056440205544338944 (G = 10.31; see Table 2). The predicted mid-time was 01:57:46 UT, the shadow geometry is shown in Fig. C.1b, and the corresponding event parameters are summarised in Table 3.

Eight stations reported positive detections, while two sites provided negative chords that contributed essential constraints on the limb geometry. In addition to this extensive campaign, the event was independently observed by Levine et al. (2021) using the 4.3-metre Lowell Discovery Telescope (LDT) near Happy Jack, Arizona, and a 0.32-metre Titan Monitor (TiMo) telescope co-mounted with the Lowell's Mars Hill 0.8-metre telescope

[3] For Ixion's ephemerides, see https://lesia.obspm.fr/lucky-star/obj.php?p=1192.
[4] https://lesia.obspm.fr/lucky-star
[5] https://occultationportal.org

Table 3. Summary of the geometric and observational parameters for all Ixion stellar occultation events.

Date (UT)	Δ (au)	v (km s^{-1})	$\theta_\star$ (mas)	S^a (km pt^{-1})	Chords	Positive	Negative	Other
28 Jul. 2023 06:13:24	37.34	20.21	0.0500	~2–20	7	3	3	1
30 Jun. 2022 00:22:52	37.46	24.66	0.0335	~25–100	8	4	1	3
2 Jun. 2022 18:09:33	37.54	23.15	0.0280	~7	1	1	0	0
17 Aug. 2021 11:36:12	38.10	12.11	0.0183	~36	1	1	0	0
20 May 2021 06:43:23	37.89	20.66	0.0320	~1–40	5	4	1	0
28 Apr. 2021 07:35:37	38.15	13.54	0.0471	~7–70	16	6	5	5
13 Oct. 2020 01:57:46	39.26	16.12	0.6750	~0.5	10	8	2	0
17 Aug. 2020 01:42:15	38.37	11.61	0.0530	~3–6	3	3	0	0

Notes. Nominal geocentric mid-time (Date, UT). Geocentric distances (Δ) and apparent sky-plane velocities (v) are evaluated at mid-event. Stellar angular diameters ($\theta_\star$) are those adopted in the light-curve modelling. S^a denotes the typical along-chord distance represented by a single photometric data point, combining exposure time with the apparent shadow velocity. 'Chords' refers to the total number of observing stations; 'Positive' indicates successful detections; 'Negative' indicates stations where no flux drop was recorded within the predicted window; and 'Other' includes stations affected by poor weather, technical problems, or incomplete/unreported observations. Detailed ingress and egress timings for all positive detections are listed in Table A.1. Star identifiers and NIMA solutions used for event predictions appear in Table 2.

in Flagstaff, Arizona. The present work incorporates a broader set of light curves and a larger number of observing stations, and the data from Levine et al. (2021) were also included to improve consistency across analyses. The overall distribution of the observation network and the predicted shadow track for this event are presented in Fig. C.1b.

Most participating observers employed video cameras synchronised via IOTA-VTI GPS time inserters, achieving subsecond timing accuracy. All stations acquired their data in clear mode, consistent with the standard configuration adopted across the campaigns. Exposure times were typically 0.033 s, providing high temporal resolution well matched to the event geometry.

Given the brightness of the occulted star, its projected angular diameter was also a relevant factor limiting the effective resolution. As Levine et al. (2021) noted, the star is classified as a mid-M giant (a classification consistent with its location in the Hertzsprung–Russell diagram; Kilic 2025a), and its angular diameter was adopted as 0.675 ± 0.010 mas, corresponding to ~19.3 km at Ixion's distance. This value was used as the initial reference diameter in our analysis and was subsequently cross-checked against our own occultation light curves, as detailed in the analysis section.

Because of the combination of short exposures, Fresnel diffraction, and the unusually large projected stellar diameter for this event, detailed modelling was required to reproduce the ingress and egress shapes. For stations using 0.033 s exposures, the finite integration time, the Fresnel scale, and the size of the stellar disc were explicitly accounted for in the timing fits.

3.3. 28 April 2021 occultation

This event was remarkable for the wide geographic extent of the observing network, with sixteen stations across Brazil, Argentina, Uruguay, and Chile participating in the campaign (see Table D.1). The occultation involved the G = 14.84 mag star Gaia DR3 4050000576486883840 (see Table 2). The predicted mid-time was 07:35:37 UT, the shadow geometry is shown in Fig. C.1c, and the corresponding event parameters are summarised in Table 3.

Among the participating sites, six successfully detected the event, while five reported negative chords that were essential for constraining the object's silhouette. The remaining stations were affected by overcast conditions and did not obtain usable data. The observing setups were highly diverse, ranging from the 1.6 m telescope at Observatório do Pico dos Dias (OPD) to smaller 20–30 cm instruments. Exposure times also spanned more than an order of magnitude, from 0.15 s to 10 s, reflecting both instrumental capabilities and observing strategies. Unlike the earlier campaigns, several sites in this observation employed moderate to long exposure times (5–10 s), which significantly smoothed ingress and egress features. However, the inclusion of faster cadence light curves from larger apertures, such as OPD and Cerro Tololo Inter-American Observatory (CTIO), mitigated these limitations and enabled precise chord fitting. Except for the CASLEO–Cerro Burek ASH station, which used a luminance (L) filter, all other observers acquired images in clear mode.

3.4. 20 May 2021 occultation

The occultation observed on 20 May 2021 involved five stations in the United States (see Table D.1). The target star was Gaia DR3 4050180170543871104 (G = 14.18; see Table 2). The predicted mid-time was 06:43:23 UT, the shadow geometry is shown in Fig. C.1d, and the corresponding event parameters are summarised in Table 3.

Four stations reported positive detections, while one site provided a negative chord. The telescopes were of moderate aperture (typically 20–40 cm), and exposure times ranged from 0.03 s to 2 s, yielding spatial samplings of order 1–2 km along the chords (sees Tables D.1 and 3). All observers acquired their data in clear mode to maximise signal-to-noise. Because the observing configurations were relatively homogeneous, the set of positive chords provided a coherent astrometric constraint; however, their tight clustering in cross-track position limited the ability to robustly constrain Ixion's limb shape. In this context, the negative chord from Westport is especially valuable: its proximity to the positive detections sharply restricts the allowed limb extent and significantly improves the silhouette constraint despite the modest network size.

3.5. 30 June 2022 occultation

The 30 June 2022 occultation was observed predominantly from Brazil, with eight stations contributing to the campaign (see Table D.1). The target star was Gaia DR3 4049905056379149824 (G = 15.0; see Table 2). The shadow geometry for this event is

shown in Fig. C.1g, and the corresponding event parameters are summarised in Table 3.

Five stations obtained usable data, with four recording positive detections of the occultation. The observing configurations were characterised by modest telescope apertures (10–40 cm), but their geographic distribution provided chords sampling different regions of the limb. Although the network size was limited, the resulting chord pattern yielded meaningful astrometric constraints. The negative chord from the Southern Observatory for Near-Earth Asteroids Research (SONEAR) is particularly valuable: its grazing geometry relative to the cluster of positive detections significantly restricts the range of admissible limb solutions and improves the overall silhouette constraint.

Exposure times ranged from 1 to 4.5 s, corresponding to effective spatial samplings of order 1–2 km once combined with diffraction and the projected stellar diameter. All observers used clear mode, consistent with the standard configuration adopted across the campaigns. Weather conditions were favourable at most sites, with only a few stations affected by cloud coverage or technical issues (see Table D.1).

3.6. 28 July 2023 occultation

The 28 July 2023 stellar occultation was monitored from seven stations in Chile, Argentina, and Brazil (see Table D.1). The occulted star was Gaia DR3 4049162851669604096 (G = 14.53; see Table 2). The shadow geometry for this event is shown in Fig. C.1h, and the corresponding event parameters are summarised in Table 3.

Of the seven observing sites, three secured clear positive detections of the occultation. Exposure times ranged from 0.1 to 10 s, and weather conditions varied between excellent transparency and localised cloud cover, affecting the success rate across sites. Notably, the positive chords originated from observatories equipped with relatively large apertures – such as the 4.1 m SOAR telescope and the 1.54 m Danish telescope at La Silla, which permit high-cadence photometry with exposures as short as 0.1–0.2 s. All stations except two acquired their data in clear mode; Danish/ESO used a red filter, and Astroquinta employed an L-eNhance filter (see Table D.1). This combination of large telescopes and fast sampling provided precise timings of ingress and egress, enhancing the accuracy of the limb reconstruction. By contrast, several smaller-aperture sites achieved only partial coverage or negative results. Despite the modest number of positive chords, their proximity in the plane of the sky offered useful constraints on Ixion's profile, albeit limiting the ability to model shape asymmetries comprehensively.

The presence of negative chords, particularly those from the Complejo Astronómico El Leoncito (CASLEO) – Cerro Burek HSH and OPD observatories, proved valuable for bounding the possible limb solutions. These non-detections passed close enough to the positive chords to significantly reduce the uncertainty in Ixion's size and centre position.

3.7. Single-chord stellar occultations

Two single-chord stellar occultations were successfully recorded in 2021 and 2022, providing useful constraints on Ixion's size and astrometric position despite their limited geometrical coverage. Both shadow paths crossed southern Australia (see Figs. C.1e and C.1f), enabling observations from well-equipped amateur and professional facilities. The identifiers of the occulted stars are listed in Table 2; event-specific geometric parameters are summarised in Table 3, and the corresponding observing configurations are given in Table D.1.

17 August 2021: the occulted star was Gaia DR3 4056220440657653248 (G = 16.9; see Table 2). The event was recorded from Heaven's Mirror Observatory (New South Wales) with a 50.8 cm telescope equipped with a QHY174M–GPS camera (Table D.1). A continuous sequence of 3.0 s exposures captured a clear flux drop, yielding a well-defined single chord under stable atmospheric conditions.

2 June 2022: the target star was Gaia DR3 4049248613603980416 (G = 15.3; see Table 2). The event was recorded from Glenlee Observatory (Australia) using a 30 cm telescope equipped with a Watec 910BD camera operating at a 0.32 s cadence. Conditions were cloudless with moderate seeing, and timing was provided by an IOTA-VTI GPS inserter (see Table D.1 for full site details). These observations yielded a nearly grazing chord of 104.3 ± 2.5 km. The grazing geometry significantly reduced the apparent stellar motion relative to the observer, requiring a dedicated determination of the effective limb-crossing speed to accurately derive the ingress and egress times.

Although single-chord events cannot constrain Ixion's full limb profile, they provide independent astrometric measurements and robust bounds on its size. Continued multi-chord campaigns remain essential to improve constraints on Ixion's shape and refine its ephemerides.

4. Data analysis and results

The stellar occultation observations analysed here were obtained during international campaigns between 2020 and 2023, involving both professional and amateur observatories equipped with telescopes from small portable instruments to 4-metre-class facilities. Details of the observing sites and acquisition parameters are provided in Appendix D, while Table 6 summarises the archival photometric dataset used to determine Ixion's absolute magnitude (H_V), phase coefficient, and geometric albedo (p_V). Data reduction and analysis were carried out using independent pipelines and photometric tools developed within the collaboration.

4.1. Data acquisition and reduction

The observational datasets collected for Ixion span a wide range of formats and image quality, including both flexible image transport system (FITS)[6] images and video-based recordings (`.avi`, `.ser`, `.adv`, `.aav`, etc.). For FITS data accompanied by calibration frames (bias, dark, and flat), a standard pre-reduction routine was applied, which performed bias subtraction, dark correction, and flat-field normalisation using well-established procedures. When video files were provided, they were first converted to FITS format through a dedicated module in the `Occultation Portal` built upon `PyMovie` using `stacker.py`. The details of this conversion pipeline are extensively described in Kilic et al. (2022) and Anderson (2019).

All resulting light curves were generated directly within the `Occultation Portal`. To ensure the reliability of these results, all datasets were independently analysed with the `PRAIA`[7] (Package for the Reduction of Astronomical Images Automatically) software (Assafin 2023), providing a cross-check with the

[6] https://fits.gsfc.nasa.gov/
[7] https://ov.ufrj.br/praia-photometry-task/

portal-generated light curves. No significant discrepancies were found.

4.2. Light-curve modelling

All positive light curves were modelled using the SORA[8] (Stellar Occultation Reduction Analysis) package (Gomes-Júnior et al. 2022). For each station, the model includes Fresnel diffraction, the finite angular size of the occulted star, the integration time of the detector, and the effective CCD bandwidth. Ingress and egress times were obtained by fitting the SORA model to each light curve, and the resulting timings with their associated 1σ uncertainties are listed in Table A.1, making use of the stellar parameters and event geometries presented in Tables 2 and 3.

Across all events, Fresnel diffraction and the projected stellar diameter are both in the 1.3–1.6 km range, comparable to one another and to the finest spatial sampling achieved in the data. The Fresnel scale is computed as $F = \sqrt{\lambda\Delta/2}$ for $\lambda = 600$ nm, yielding $F \simeq 1.3$–1.4 km over the geocentric distance interval $\Delta \simeq 37.8$–39.3 au. Typical exposure times of 0.1–0.4 s correspond to along-chord resolutions of ∼2.5–4.5 km for Ixion's sky-plane velocities ($v \simeq 10$–$25\,\mathrm{km\,s^{-1}}$), while the fastest observations (0.033 s cadence) reach $\lesssim$1 km sampling, allowing diffraction and finite-star effects to be directly resolved.

Except for the 17 August 2021 event, all occulted stars lie in the giant regime of the Hertzsprung–Russell diagram (see Kilic 2025a). Their angular diameters were therefore derived using the giant-star calibration of the van Belle (1999) surface-brightness relations, ensuring a uniform and internally consistent treatment across campaigns. The 17 August 2021 star lies on the main sequence and was modelled using the corresponding van Belle coefficients. In all cases, the resulting angular diameters were converted into projected sizes at Ixion's geocentric distance and used as fixed inputs in the SORA light-curve fits.

Refined stellar diameter estimates from the 13 October 2020 event

As described in Sect. 3.2, the 13 October 2020 event involved Ixion occulting a relatively bright star ($G = 10.31$ mag), Gaia DR3 4056440205544338944. Because of the star's brightness and Ixion's geocentric distance (39.26 au), the projected stellar diameter (hereafter simply 'stellar diameter') was a key factor to account for during the modelling process. The Occultation Portal data were obtained using various instruments, primarily small-aperture telescopes, resulting in light curves with different S/N levels. Consequently, the stellar diameter derived from each chord showed minor variations but remained consistent within the uncertainties.

To determine the stellar diameter for each chord, we applied a χ^2 minimisation approach (Gomes-Júnior et al. 2022):

$$\chi^2 = \sum_{i=1}^{N} \left(\frac{(\phi_{i,obs} - \phi_{i,cal})^2}{\sigma_i^2} \right). \tag{1}$$

The parameter scan was performed over the range 9.00 km $\leq d_\star \leq$ 30.00 km with a step size of $\Delta d_\star = 0.25$ km, and the values satisfying $\chi^2 < \chi^2_{\min} + \Delta\chi^2$ at the 3σ confidence level were selected.

From the set of stellar diameters d_i obtained for each chord (each with its associated uncertainty σ_i), we derived the weighted mean stellar diameter using

$$d_\star = \frac{\sum_{i=1}^{n} \frac{d_i}{\sigma_i^2}}{\sum_{i=1}^{n} \frac{1}{\sigma_i^2}}, \tag{2}$$

where n is the total number of chords. The corresponding uncertainty of the weighted mean was calculated as

$$\sigma_\star = \left(\sum_{i=1}^{n} \frac{1}{\sigma_i^2} \right)^{-\frac{1}{2}}. \tag{3}$$

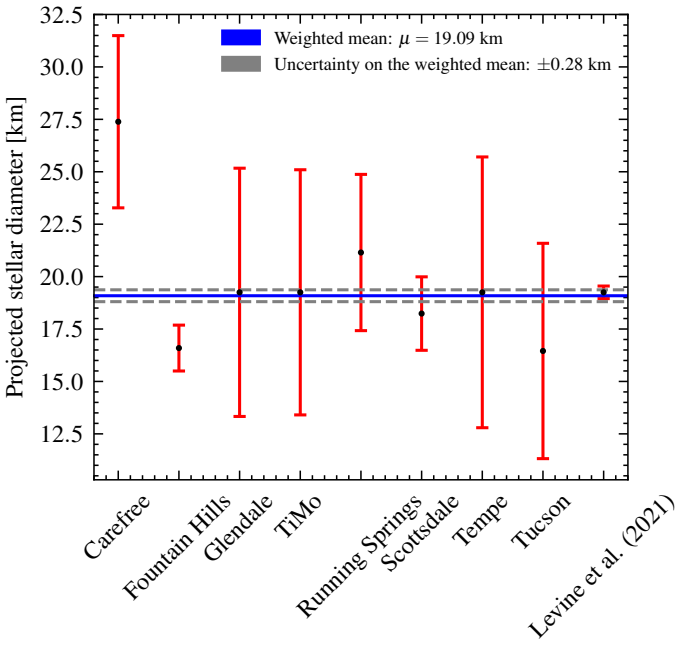

Fig. 1. Stellar diameter estimates for the occulted star Gaia DR3 4056440205544338944, obtained by scanning models across the observed light curves of the 13 October 2020 occultation. The weighted mean of all results is $\mu = 19.09 \pm 0.28$ km, shown with a 3σ confidence interval. Data from Levine et al. (2021) were also included in the final estimate. The error bars represent the uncertainties derived from model fits to each chord.

As illustrated in Fig. 1, the light curve with the lowest uncertainty was obtained by Levine et al. (2021) using the 4.3 m LDT. The relative flux dispersion in this light curve is <0.1, making it the most precise measurement and thus the largest contributor to the weighted mean. Most other light curves were obtained with small telescopes (20–30 cm apertures) under the *Lucky Star* campaign (see Table D.1).

The final weighted mean angular diameter of the occulted star Gaia DR3 4056440205544338944 is $\theta_\star = 0.670 \pm 0.010$ mas, corresponding to a projected linear diameter of 19.09 ± 0.28 km at Ixion's distance of 39.26 au. This represents a remarkably precise angular size determination from a TNO occultation and is entirely consistent with the value derived by Levine et al. (2021, 19.25 ± 0.30 km). Combining our result with the star's *Gaia* parallax (0.5645 ± 0.0417 mas) yields a physical stellar radius of $128 \pm 10\,R_\odot$, also consistent with Levine et al. (2021, $130^{+20}_{-17}\,R_\odot$).

Gaia DR3 provides stellar radii inferred by the GSP-Phot module[9] (Creevey et al. 2023), which uses multiple

[8] https://sora.readthedocs.io/latest/overview.html

[9] General Stellar Parametrizer from Photometry.

stellar-atmosphere libraries within the Aeneas algorithm (see Andrae et al. 2023). In the main *Gaia* DR3 catalogue, only a single 'best' solution is published for each source. For Gaia DR3 4056440205544338944, this default solution corresponds to the OB-library model, which yields a radius of $\sim 56\,R_\odot$ (which corresponds to an angular diameter of $\theta_\star \simeq 0.29$ mas), i.e. more than a factor of two smaller than our occultation-based estimate. However, the *Gaia* DR3 supplementary GSP-Phot results for the same source provide alternative solutions derived from different stellar libraries. In particular, the MARCS-library solution returns a radius of $\sim 116\,R_\odot$ ($\theta_\star \simeq 0.61$ mas), much closer to the 0.670 ± 0.010 mas angular diameter that we obtain from the occultation. This indicates that the apparent tension arises primarily from the automatic library selection in the GSP-Phot module (Aeneas algorithm) rather than from an intrinsic inconsistency between *Gaia* and the occultation result. For cool, luminous late-type giants, the module may select as 'best' a solution based on a library that is not optimal for this spectral regime, while an alternative library (e.g. MARCS) yields a physically more plausible radius (Sect. 2.6 of Andrae et al. 2023).

4.3. Limb fitting and astrometry

The ingress and egress times derived from all positive detections (see Table A.1) were projected onto the sky plane to reconstruct the silhouette of (28978) Ixion during each event. These timings were analysed with the `SORA` package (Gomes-Júnior et al. 2022), using a sharp-edge occultation model that accounts for the finite stellar diameter, Fresnel diffraction, exposure-time smearing, and CCD bandwidth. Negative chords, when available, were incorporated via the `filter_negative_chord` function to constrain the limb geometry further. When negative chords are present, they naturally restrict the family of acceptable limb solutions, which may clip the outer portions of the 1σ confidence region in Fig. E.2, as occurs for events with constraining non-detections (e.g. 28 April 2021, 20 May 2021, and 30 June 2022).

For the multi-chord events (17 August 2020, 13 October 2020, 28 April 2021, 20 May 2021, 30 June 2022, and 28 July 2023), the observed limb was modelled as an ellipse defined by five free parameters: the centre offsets (f, g) with respect to the NIMA v13 prediction ephemeris, the apparent equatorial radius $R_{\rm equatorial} = a$, the apparent oblateness $\epsilon' = (a - b)/a$, and the position angle of the minor axis, denoted by ϕ and defined as the angle measured eastwards from celestial north. The statistical significance of the fits was evaluated through the reduced chi-square $\chi^2_{\rm pdf} = \chi^2/(N - M)$, where N is the number of fitted points and $M = 5$ the number of free parameters. The 1σ uncertainties for each parameter were obtained by varying the parameter around its nominal value until $\chi^2 = \chi^2_{\rm min} + 1$.

Given that several events have only a limited number of chords or exhibit significant timing uncertainties, a purely free fit may yield poorly constrained position angles. To mitigate this, we adopted a strategy inspired by Braga-Ribas et al. (2013, 2014), Benedetti-Rossi et al. (2016), Ortiz et al. (2017), Dias-Oliveira et al. (2017), and Rizos et al. (2025), where ϕ is allowed to vary freely but within a physically plausible interval guided by the best-constrained events. In particular, the 13 October 2020, 28 April 2021, and 30 June 2022 occultations, which provide the most reliable constraints, yielded ϕ values of $34.1° \pm 15.7°$, $35.3° \pm 17.5°$, and $29.1° \pm 11.7°$, respectively. These values are mutually consistent, defining a preferred range of approximately 25°–40° for Ixion's apparent limb orientation. For other events, our fits were guided by this range, ensuring convergence towards physically meaningful solutions without imposing a strict fixed ϕ.

The projection of single chords onto the sky plane yields two symmetrical solutions for the centre position along the direction perpendicular to the chord, leaving the limb shape unconstrained. For this reason, the single-chord events (17 August 2021 and 2 June 2022) are used only to derive the astrometric offsets (f, g), while the limb parameters (a, b, ϕ) are fixed to the global multi-chord solution. Although the 17 August 2021 chord is notably long (~770 km), single-chord geometries do not permit a reliable size estimate, and we therefore do not derive any diameter constraints from these events.

The results of all ellipse fits are summarised in Table 4, which lists the derived (f, g) offsets, equatorial and polar radii, apparent oblateness, ϕ, equivalent radius, radial dispersion, and $\chi^2_{\rm pdf}$. Visual representations of the fitted limbs are shown in Fig. E.2 (panels a–h).

4.4. Global limb fit

We derived a global limb solution for (28978) Ixion by jointly fitting all multi-chord stellar occultations observed between 2020 and 2023 using a per-event centre minimisation approach. In this framework, Ixion's apparent limb is described by a single projected ellipse, while the astrometric centre of each occultation event is optimised independently.

The global shape parameters, defined by the semi-axes (a, b) and the position angle (ϕ; measured eastwards from celestial north, modulo 180°), were explored using a Monte Carlo sampling of the 3D (a, b, ϕ) parameter space, centred on physically motivated initial values. For each Monte Carlo realisation, the astrometric centres of all events were re-optimised by minimising the event-wise contributions to the total χ^2. The global goodness of fit was then computed as the sum of these event-wise χ^2 values.

Allowing independent astrometric centres for each event prevents ephemeris or astrometric offsets from biasing the inferred global limb parameters, ensuring that the shape solution is driven by the relative geometry of the chord extremities rather than by systematic offsets between observing epochs. In addition, a small extra model uncertainty of $\sigma_{\rm model} = 4$ km was added in quadrature to the uncertainties of the chord extremities in the projected f–g plane, in order to account for possible un-modelled limb effects or small-scale topography (Rommel et al. 2023).

The final confidence intervals were derived from the ensemble of accepted Monte Carlo solutions within a $\Delta\chi^2$ threshold of $\Delta\chi^2 = 3.53$, appropriate for three global shape parameters. The total number of free parameters in the fit is therefore $M = 3 + 2N_{\rm events}$, corresponding to the global ellipse parameters and the per-event astrometric centres. The resulting fit involves $N_{\rm data} = 56$ chord extremities and $\nu = 41$ degrees of freedom, yielding a reduced $\chi^2_\nu = 1.17$, consistent with the expected statistical distribution given the adopted observational and model uncertainties.

The best-fitting global solution is

$$a = 363.42^{+3.53}_{-3.85}\ \text{km}, \quad b = 333.98^{+7.07}_{-4.96}\ \text{km}, \quad \phi = 110.97^{+7.00}_{-6.54}\ \text{deg}, \tag{4}$$

where the quoted uncertainties correspond to asymmetric 1σ confidence intervals derived from the χ^2 surface. From these values, we derived an equivalent radius based on the projected area,

Table 4. Best-fitted limb solutions for (28978) Ixion (1σ uncertainties) derived from stellar occultations.

Parameter	17 Aug. 2020	13 Oct. 2020	28 Apr. 2021	20 May 2021	17 Aug. 2021	2 Jun. 2022	30 Jun. 2022	28 Jul. 2023
f (km)	1.7 ± 7.6	−8.0 ± 1.4	−41.6 ± 7.6	−71.7 ± 31.2	−8.3 ± 18.4	30.3 ± 75.6	−38.5 ± 16.6	−132.0 ± 9.8
g (km)	5.4 ± 7.2	4.6 ± 5.8	1.8 ± 4.4	48.7 ± 110.8	19.5 ± 47.6	−31.6 ± 15.7	−27.0 ± 7.2	−47.6 ± 55.1
$R_{\rm equatorial}$ (km)	375.1 ± 11.7	366.8 ± 6.2	391.9 ± 9.4	375.9 ± 20.8	–	–	389.5 ± 16.8	371.1 ± 33.5
$R_{\rm polar}$ (km)	330.2 ± 20.1	346.1 ± 7.4	322.2 ± 17.2	338.2 ± 41.6	–	–	325.6 ± 31.5	334.0 ± 47.8
ϵ'	0.120 ± 0.046	0.056 ± 0.012	0.231 ± 0.102	0.100 ± 0.099	–	–	0.16 ± 0.072	0.100 ± 0.100
ϕ (°)	14.86 ± 8.10	34.11 ± 15.70	35.25 ± 17.50	−4.23 ± 63.65	–	–	31.35 ± 13.51	−0.04 ± 89.81
$R_{\rm equiv}$ (km)	351.9 ± 12.0	356.3 ± 4.9	386.3 ± 59.8	356.6 ± 24.1	–	–	356.1 ± 18.9	352.0 ± 29.8
$R_{\rm dispersion}$ (km)	−0.23 ± 5.89	−1.87 ± 2.83	−6.79 ± 8.83	−21.1 ± 6.18	–	–	−3.77 ± 10.85	−12.2 ± 8.6
$\chi^2_{\rm pdf}$	0.816	0.926	0.393	0.303	–	–	0.098	0.938
Ellipse fit	Fig. E.2a	Fig. E.2b	Fig. E.2c	Fig. E.2d	Fig. E.2e	Fig. E.2f	Fig. E.2g	Fig. E.2h

Notes. For the single-chord events (17 August 2021 and 2 June 2022), only the astrometric offsets (f, g) were fitted; the limb shape parameters were fixed to the global multi-chord solution.

$$R_{\rm equiv} = \sqrt{ab} = 348.39^{+5.37}_{-4.43}\ \text{km}, \tag{5}$$

which corresponds to an equivalent diameter

$$D_{\rm equiv} = 696.78^{+10.75}_{-8.87}\ \text{km}. \tag{6}$$

The apparent oblateness is

$$\epsilon' = \frac{a-b}{a} = 0.081^{+0.004}_{-0.010}, \tag{7}$$

indicating a moderately flattened projected shape.

The resulting global limb solution is illustrated in Fig. 2, where the best-fitting ellipse and its 1σ uncertainty envelope are shown together with the chord extremities from all observing epochs; the corresponding orthogonal residuals are presented in Appendix E.3.

4.5. Astrometry

The astrometric solutions for (28978) Ixion derived from eight stellar occultations between 2020 and 2023 are summarised in Table 5. For each event, the ellipse fit provides the centre coordinates (offsets X, Y) relative to the predicted position, defined by the object's ephemeris and the star coordinates. These offsets were used to determine the precise International Celestial Reference System (ICRS) equatorial coordinates of Ixion at the occultation mid-time (see Table 5).

The sub-milliarcsecond precision achieved in most events is a direct consequence of the accurate timing of the occultation light curves combined with the *Gaia* DR3 catalogue positions of the occulted stars. These eight astrometric measurements will be incorporated into the orbital refinement of Ixion, improving its ephemeris and the accuracy of future stellar occultation predictions.

4.6. Archival photometry: H_V, G, and p_V

We analysed the photometric properties of (28978) Ixion using archival observations. A total of 39 raw V-band images obtained with the New Technology Telescope (NTT) equipped with the ESO Multi-Mode Instrument (EMMI) were retrieved from the ESO archive[10], together with two V-band images from the Very

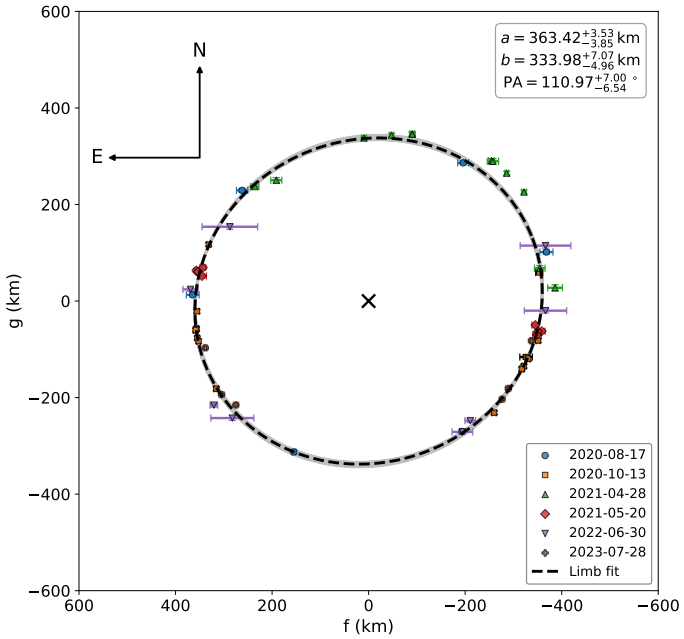

Fig. 2. Global limb fit of (28978) Ixion obtained by combining the chord extremities from all multi-chord stellar occultations observed between 2020 and 2023. Each colour and marker shape corresponds to a different event (see the legend). The dashed black curve shows the best-fitting ellipse derived from the global χ^2 minimisation, while the grey-shaded region represents the 1σ uncertainty envelope of the global limb solution. Error bars represent the projected uncertainties of the chord extremities in the f–g plane (in kilometres). The black x marks the limb-centred reference frame, and the arrows indicate the celestial north (N) and east (E) directions. The data used in this figure are available in Kilic (2025b).

Large Telescope (VLT) using the FOcal Reducer and low dispersion Spectrograph 1 (FORS1)[11]. In addition, 14 unique measurements of Ixion were extracted from the 138 available data of Ixion in the *Gaia* DR3 database (Gaia Collaboration 2023), and one additional V-band magnitude reported by (Boehnhardt et al. 2004) was included to improve the phase-angle coverage (see Table 6).

From the 39 NTT frames, 28 images were selected based on focus, tracking quality, S/N and minimal contamination from background sources. The ESO data were first processed

[10] ESO programme ID 075.C-0431(A).

[11] ESO programme ID 178.C-0036(N).

Table 5. Astrometric solutions for (28978) Ixion derived from stellar occultations.

Date (UT)	Time (UT)	RA (hh mm ss.s)	Dec (dd mm ss.s)	Offset X (km)	Offset Y (km)
2020-08-17	01:37:11.820	$17^h49^m53.5853^s \pm 0.284$ mas	$-29°48'12.3881^s \pm 0.282$ mas	1.7 ± 7.6	5.4 ± 7.2
2020-10-13	01:57:46.320	$17^h50^m20.3585^s \pm 0.141$ mas	$-29°43'32.9060^s \pm 0.274$ mas	-8.0 ± 1.4	4.6 ± 5.8
2021-04-28	07:36:45.400	$18^h05^m34.6798^s \pm 0.567$ mas	$-30°09'09.7432^s \pm 0.240$ mas	-41.6 ± 7.6	1.8 ± 4.4
2021-05-20	06:43:21.420	$18^h04^m05.2324^s \pm 1.200$ mas	$-30°13'44.4493^s \pm 3.868$ mas	-71.7 ± 31.2	48.7 ± 110.8
2021-08-17	11:36:10.400	$17^h56^m18.8131^s \pm 1.030$ mas	$-30°17'43.7814^s \pm 2.120$ mas	-8.3 ± 18.4	19.5 ± 47.6
2022-06-02	18:09:30.140	$18^h09^m36.9353^s \pm 2.783$ mas	$-30°43'37.0537^s \pm 0.616$ mas	30.3 ± 75.6	-31.6 ± 15.7
2022-06-30	00:22:49.920	$18^h06^m53.6124^s \pm 0.642$ mas	$-30°46'56.5116^s \pm 0.351$ mas	-38.5 ± 16.6	-27.0 ± 7.2
2023-07-28	06:13:19.080	$18^h11^m03.2660^s \pm 0.399$ mas	$-31°15'22.5483^s \pm 2.046$ mas	-132.0 ± 9.8	-47.6 ± 55.1

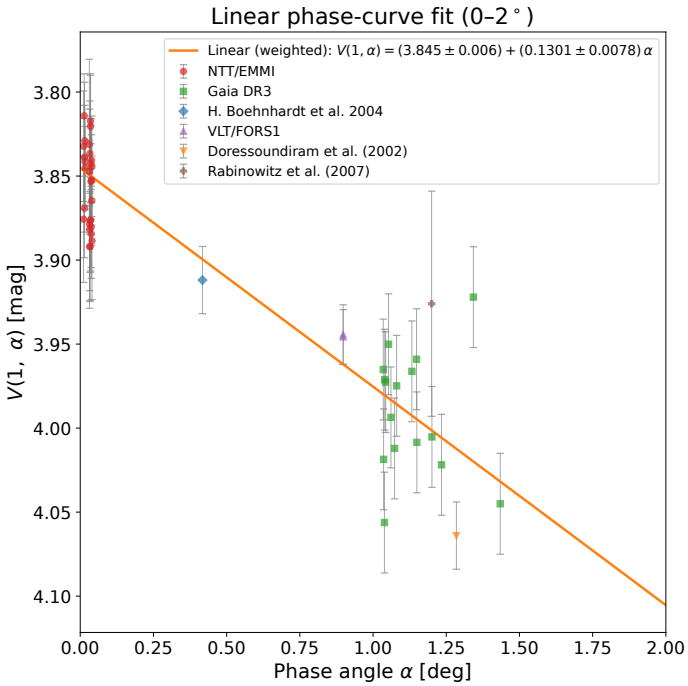

Fig. 3. Linear phase-curve fit for Ixion in the restricted 0–2° phase angle range (datasets listed in Table 6).

through standard pre-reduction procedures, and apparent magnitudes were derived using the *PhoPS* algorithm (Erece et al. 2023). For the *Gaia* data, the G magnitudes were transformed into V magnitudes using the equations published by Carrasco & Bellazzini (2022). Reduced magnitudes, $V(1, \alpha)$, normalised to $r = \Delta = 1$ AU, were then computed as

$$V(1, \alpha) = V - 5 \log(r\Delta), \tag{8}$$

where r and Δ denote the heliocentric and geocentric distances, respectively

Because such distant objects cannot be observed over a wide range of phase angles, we modelled the phase curve in the restricted range 0–2° with a linear relation, $V(1, \alpha) = H + \beta\,\alpha$. The fit yields $H = 3.845 \pm 0.006$ and a slope $\beta = 0.1301 \pm 0.0078$ mag deg^{-1} (Fig. 3).

We also retrieved B, R, and I magnitudes from the NTT/EMMI data to derive colour indices for Ixion. To minimise effects related to rotation, phase angle, or distance, we used measurements obtained closest in time. We derived $B - V = 1.06 \pm 0.03$, $V - R = 0.61 \pm 0.02$, and $R - I = 0.54 \pm 0.03$, values consistent with the red spectral slope typically observed among TNOs, and in good agreement with previous results published by Boehnhardt et al. (2004).

Using the equivalent radius derived from the global limb fit (Sect. 4.4), we re-estimated Ixion's geometric albedo in the visible band.The best-fitting ellipse obtained from the combined multi-chord occultations (2020–2023) yields an equivalent radius of $R_{\rm equiv} = 348.39^{+5.37}_{-4.43}$ km, corresponding to an equivalent diameter of $D_{\rm equiv} = 696.78^{+10.75}_{-8.87}$ km. Combining this size with our determination of the absolute magnitude, $H_V = 3.845 \pm 0.006$, we derived the geometric albedo p_V using the classical relation introduced by Russell (1916), expressed with a modern calibration constant C (e.g. $C = 1330 \pm 18$ km; Masiero et al. 2021):

$$p_V = \left(\frac{C}{D_{\rm equiv}}\right)^2 10^{-0.4 H_V}. \tag{9}$$

This calculation yields a visible geometric albedo of $p_V = 0.106^{+0.003}_{-0.003}$, indicating that Ixion's surface is slightly darker than previously estimated. The result remains fully consistent within uncertainties with earlier determinations, such as the $p_V = 0.108 \pm 0.002$ value reported by Verbiscer et al. (2022), and confirms that Ixion lies among the brighter members of the Plutino population.

5. Discussion and conclusions

Our analysis indicates a moderately elongated body with an area-equivalent diameter of $D_{\rm equiv} = 696.78^{+10.75}_{-8.87}$ km and a visible geometric albedo of $p_V = 0.106^{+0.003}_{-0.003}$. According to the colour–albedo distribution presented by Lacerda et al. (2014, their Fig. 2), Ixion lies between the dark-neutral and bright red groups, ranking among the brighter members of the Plutino population. The absolute magnitude we derive ($H_V = 3.845 \pm 0.006$) is slightly fainter than the value reported by Alvarez-Candal et al. (2016, $H_V = 3.774 \pm 0.021$), likely reflecting the broader temporal coverage of our dataset and the consequent mitigation of rotational-phase bias. Although no secure rotational period could be established, the scatter in both the light curves and the residuals of the phase-curve fit suggest slight departures from axial symmetry and/or heterogeneous surface properties, as expected for objects of this size (e.g. Duffard et al. 2009).

The global limb fit (Sect. 4.4) shows that the chord extremities from the 2020–2023 occultation campaigns are well reproduced, to first order, by a single projected ellipse. No evidence

Table 6. Observational data used in this study.

Telescope/Inst.	Date (UT)	Filter	N_{obs} used/total	Exp. time (s)	Apparent mag (V)	Phase angle (°)	Notes
NTT/EMMI	2005-05-29	B	3/28	360	21.15	0.9	Prog. ID 075.C-0431(A)
NTT/EMMI	2005-05-29/30/31	V	28/39	120	20.08	0.01–0.04	Prog. ID 075.C-0431(A)
NTT/EMMI	2005-05-29	R	12/20	120	19.47	0.9	Prog. ID 075.C-0431(A)
NTT/EMMI	2005-05-29	I	3/12	60	18.91	0.9	Prog. ID 075.C-0431(A)
VLT/FORS1	2007-07-14	V	2/2	40	20.14	0.90	Prog. ID 178.C-0036(N)
Gaia DR3	2014–2017	G	14/14	–	19.61–19.81	0.5–1.4	Gaia Collaboration (2023)
CFHT	2002-08-12	V	1/1	–	20.39	1.28	Doressoundiram et al. (2002)
VLT/FORS1	2002-05-11	V	1/1	–	20.21	0.42	Boehnhardt et al. (2004)
SMARTS/ANDICAM	2003-03-25	V	1/1	–	–	1.20	Rabinowitz et al. (2007)

Notes. Apparent magnitudes correspond to average values per dataset. Phase angle refers to the Sun–Ixion–Earth angle at the time of observation.

of systematic trends is found in the residuals, and the reduced χ^2_ν close to unity indicates a statistically acceptable fit given the adopted observational and model uncertainties. The derived apparent oblateness, $\epsilon' = 0.081^{+0.004}_{-0.010}$, is consistent with a moderately flattened projected figure, providing an adequate first-order description of Ixion's global shape.

While the majority of occultation epochs are mutually consistent with this global limb solution, the events of 28 April 2021 and 30 June 2022 exhibit noticeable offsets relative to the best-fitting projected ellipse. These deviations are not indicative of shortcomings in the modelling approach but may reflect changes in the projected figure of the body sampled at different rotational phases or aspect angles. In the absence of a well-constrained rotational period, such epoch-dependent variations are naturally expected for a body that departs slightly from axial symmetry, which is consistent with a mildly triaxial figure. The lack of any systematic trend in the residuals for the remaining well-constrained events (Appendix E.3), together with their limited scatter (typically at the ∼10 km level), supports the interpretation that a modestly flattened figure provides an adequate global description of Ixion's shape, while allowing for small departures from perfect axisymmetry.

A unique outcome of this work is the precise measurement of the angular diameter of the occulted star Gaia DR3 4056440205544338944: $\theta_\star = 0.670 \pm 0.010$ mas, which corresponds to a physical stellar radius of $128 \pm 10\,R_\odot$. This rare, direct constraint on the size of an M III giant at a distance of ∼1.7 kpc is remarkable, as such measurements are typically limited to much closer giants observed with interferometry or lunar occultations (e.g. White & Feierman 1987; Nordgren et al. 1999; Baines et al. 2016, 2018). This result also reveals a significant discrepancy with the *Gaia* DR3 GSP-Phot 'best' estimate obtained from the OB-library model (∼56 $R_\odot$, $\theta \simeq 0.29$ mas); the alternative MARCS-library solution (∼116 $R_\odot$, $\theta \simeq 0.61$ mas) is in much better agreement with our occultation-based value. This confirms that the apparent mismatch stems primarily from the automatic library selection in the GSP-Phot module rather than from an intrinsic inconsistency between *Gaia* and the occultation result. Consequently, multi-chord stellar occultations by TNOs can serve not only to constrain the physical properties of the occulting bodies, but also to independently validate *Gaia*-derived stellar radii in the cool-giant regime.

In addition, our analysis of detection limits (see Appendix B) shows no evidence of rings or other circum-object material around Ixion. The sensitivity of our light curves, particularly the April 2021 event observed from OPD, rules out opaque structures wider than a few hundred metres in the sky plane and constrains tenuous material with optical depths (τ) > 0.1 at kilometre scales. These limits are stringent enough that the dense rings of Chariklo, as well as those observed around Haumea and Quaoar, would have been detected if present. Thus, our results indicate that Ixion lacks ring systems or significant debris within the probed radial ranges, providing an essential negative constraint in the comparative study of small ring-bearing bodies.

Another key outcome of this work was the derivation of precise astrometric positions for Ixion. The eight multi-chord events provided sub-milliarcsecond accuracy, thanks to the combination of accurate timing and *Gaia* DR3 star catalogues (Table 5). These astrometric constraints offer valuable input for orbit refinement and will enhance the accuracy of future occultation predictions, underscoring the dual contribution of these observations to both physical and dynamical studies of TNOs.

Future progress will rely on improved photometric coverage around opposition, denser occultation campaigns, and complementary thermal radiometry. In particular, determining a reliable rotational period remains a key issue, as our re-analysis of all available datasets revealed no statistically significant periodicity. Such data will allow us to constrain Ixion's phase curve, spin state, and 3D shape more accurately, and to refine surface property estimates within the context of the broader trans-Neptunian population.

Acknowledgements. We dedicate this paper to the memory of C.A. Colesanti†, J. Pollock†, and T. George†, whose commitment, passion, and careful work in the field of occultation astronomy remain an inspiration to us all. Their contributions have enriched this study and the broader community, and their legacy will continue to guide future observations. We thank the anonymous referee for their careful review and constructive suggestions, which have helped us to improve the clarity and overall quality of the manuscript. Multiple funding agencies and institutions supported this work. It was partly funded by the Spanish projects PID2020-112789GB-I00 (AEI) and Proyecto de Excelencia de la Junta de Andalucía PY20-01309. This study was financed in part by the Coordenação de Aperfeiçoamento de Pessoal de Nível Superior – Brasil (CAPES) – Finance Code 001. J.L.O., P.S.-S., N.M., A.A.C, R.D., Y.K., J.L.R., and J.M.L.G. acknowledge financial support from the Severo Ochoa grant CEX2021-001131-S (MCIN/AEI/10.13039/501100011033). F.B.-R. acknowledges CNPq (grant 316604/2023-2) and the financial support of the NAPI "Fenômenos Extremos do Universo" of Fundação de Apoio à Ciência, Tecnologia e Inovação do Paraná. P.S.-S. and Y.K. also acknowledge support from the Spanish I+D+i project PID2022-139555NB-I00 (TNO-JWST) funded by MCIN/AEI/10.13039/501100011033. This work has been supported by the French ANR project Roche, number ANR-23-CE49-0012. J.L.R. acknowledges financial support from grant PID2021-126365NB-C21. AAC acknowledges financial support from the project PID2023-153123NB-I00 funded by MCIN/AEI. J.M.G.L. acknowledges funding by the Spanish Ministry of Universities through the university training programme FPU2022/00492. BEM thanks

CAPES Grant 23079.212658/2024-30. ARGJ thanks the financial support of FAPEMIG APQ-02987-24. This work is partly based on observations collected at the Centro Astronómico Hispano en Andalucía (CAHA), Observatorio de Sierra Nevada (IAA-CSIC), and the Liverpool Telescope at the Roque de los Muchachos Observatory (IAC). LMC thanks CAPES for the financial support, Finance Code 001, and 88881.981125/2024-01. Based on data acquired at Complejo Astronómico El Leoncito, operated under agreement between the Consejo Nacional de Investigaciones Científicas y Técnicas de la República Argentina and the National Universities of La Plata, Córdoba and San Juan. We also thank T. Linder for his valuable contribution to the 2021 April 28 observation of Ixion, performed with the CTIO 1-meter telescope, which provided important constraints for this study. Based on observations collected at the La Silla European Southern Observatory. TRAPPIST is funded by the Belgian F.R.S.-FNRS under grant PDR T.0120.21. EJ is Director of Research at the Belgian F.R.S.-FNRS. This research has made use of data from the European Space Agency (ESA) mission *Gaia* (https://www.cosmos.esa.int/gaia), processed by the Gaia Data Processing and Analysis Consortium (https://www.cosmos.esa.int/web/gaia/dpac/consortium), with funding provided by institutions participating in the Gaia Multilateral Agreement. CLP thanks the FAPERJ/DSC-10 E-26/204.141/2022, FAPERJ/PDR-10 E-26/200.107/2025, and FAPERJ 200.108/2025. This work was supported by the project Gaia Moons of the Agence Nationale de Recherche (France), grant ANR-22-CE49-0002.

References

Altenhoff, W. J., Bertoldi, F., & Menten, K. M. 2004, A&A, 415, 771
Alvarez-Candal, A., Pinilla-Alonso, N., Ortiz, J. L., et al. 2016, A&A, 586, A155
Anderson, B. 2019, J. Occult. Astron., 9, 9
Andrae, R., Fouesneau, M., Sordo, R., et al. 2023, A&A, 674, A27
Assafin, M. 2023, Planet. Space Sci., 239, 105816
Baines, E. K., Döllinger, M. P., Guenther, E. W., et al. 2016, AJ, 152, 66
Baines, E. K., Armstrong, J. T., Schmitt, H. R., et al. 2018, AJ, 155, 30
Barkume, K. M., Brown, M. E., & Schaller, E. L. 2008, AJ, 135, 55
Benedetti-Rossi, G., Sicardy, B., Buie, M. W., et al. 2016, AJ, 152, 156
Bertoldi, B., Altenhoff, W., & Junkes, N. 2002, Beyond Pluto: Max-Planck radioastronomers measure the sizes of distant minor planets, https://astro.uni-bonn.de/~bertoldi/press/kbo/pr_kbo_e.html
Boehnhardt, H., Bagnulo, S., Muinonen, K., et al. 2004, A&A, 415, L21
Braga-Ribas, F., Sicardy, B., Ortiz, J. L., et al. 2013, ApJ, 773, 26
Braga-Ribas, F., Sicardy, B., Ortiz, J. L., et al. 2014, Nature, 508, 72
Braga-Ribas, F., Pereira, C. L., Sicardy, B., et al. 2023, A&A, 676, A72
Braga-Ribas, F., Vachier, F., Desmars, J., Margoti, G., & Sicardy, B. 2025, Philos. Trans. Roy. Soc. Lond. Ser. A, 383, 20240200
Brown, M. E. 2008, in The Solar System Beyond Neptune, eds. M. A. Barucci, H. Boehnhardt, D. P. Cruikshank, A. Morbidelli, & R. Dotson (University of Arizona Press), 335
Carrasco, J. M., & Bellazzini, M. 2022, Gaia DR3 documentation: Photometric relationships with other photometric systems, https://gea.esac.esa.int/archive/documentation/GDR3/Data_processing/chap_cu5pho/cu5pho_sec_photSystem/cu5pho_ssec_photRelations.html#Ch5.T8e, accessed: 23 September 2025
Creevey, O. L., Sordo, R., Pailler, F., et al. 2023, A&A, 674, A26
Cruikshank, D. P., Barucci, M. A., Emery, J. P., et al. 2007, in Protostars and Planets V, eds. B. Reipurth, D. Jewitt, & K. Keil, 879
Desmars, J., Camargo, J. I. B., Braga-Ribas, F., et al. 2015, A&A, 584, A96
Dias-Oliveira, A., Sicardy, B., Ortiz, J. L., et al. 2017, AJ, 154, 22
Doressoundiram, A., Peixinho, N., Moullet, A., et al. 2007, AJ, 134, 2186
Doressoundiram, A., Peixinho, N., de Bergh, C., et al. 2002, AJ, 124, 2279
Duffard, R., Ortiz, J. L., Thirouin, A., Santos-Sanz, P., & Morales, N. 2009, A&A, 505, 1283
Elliot, J. L., Person, M. J., Zuluaga, C. A., et al. 2010, Nature, 465, 897
Erece, O., Khamitov, I. M., Kaplan, M., et al. 2023, Planet. Space Sci., 232, 105698
Fernández-Valenzuela, E., Ortiz, J. L., Holler, B. J., et al. 2025, Nat. Commun., 16, 10926
Gaia Collaboration (Brown, A. G. A., et al.) 2016a, A&A, 595, A2
Gaia Collaboration (Prusti, T., et al.) 2016b, A&A, 595, A1
Gaia Collaboration (Brown, A. G. A., et al.) 2018, A&A, 616, A1
Gaia Collaboration (Vallenari, A., et al.) 2023, A&A, 674, A1
Galiazzo, M., de la Fuente Marcos, C., de la Fuente Marcos, R., et al. 2016, Astrophys. Space Sci., 361, 212
Gomes-Júnior, A. R., Morgado, B. E., Benedetti-Rossi, G., et al. 2022, MNRAS, 511, 1167
Grundy, W., Noll, K., & Stephens, D. 2005, Icarus, 176, 184
Grundy, W., Noll, K., Buie, M., et al. 2019, Icarus, 334, 30
Kilic, Y. 2025a, https://doi.org/10.5281/zenodo.17524000
Kilic, Y. 2025b, https://doi.org/10.5281/zenodo.17901912
Kilic, Y., Braga-Ribas, F., Kaplan, M., et al. 2022, MNRAS, 515, 1346
Lacerda, P., Fornasier, S., Lellouch, E., et al. 2014, ApJ, 793, L2
Leiva, R., Sicardy, B., Camargo, J. I. B., et al. 2017, AJ, 154, 159
Leiva, R., Buie, M. W., Keller, J. M., et al. 2020, PSJ, 1, 48
Lellouch, E., Santos-Sanz, P., Lacerda, P., et al. 2013, A&A, 557, A60
Levine, S. E., Zuluaga, C. A., Person, M. J., et al. 2021, AJ, 161, 210
Lykawka, P. S., & Mukai, T. 2008, AJ, 135, 1161
Malhotra, R. 1995, AJ, 110, 420
Masiero, J. R., Wright, E. L., & Mainzer, A. K. 2021, PSJ, 2, 32
Minor Planet Center 2002, Minor Planet Circulars (MPC), available at: https://www.minorplanetcenter.net/iau/ECS/MPCArchive/2002/MPC_20020328.pdf [Accessed: January 11, 2025]
Mommert, M. 2013, PhD thesis, Freie Universität Berlin
Morbidelli, A., Levison, H. F., & Gomes, R. 2008, in The Solar System Beyond Neptune, eds. M. A. Barucci, H. Boehnhardt, D. P. Cruikshank, A. Morbidelli, & R. Dotson (arXiv), 275
Morgado, B. E., Sicardy, B., Braga-Ribas, F., et al. 2021, A&A, 652, A141
Morgado, B. E., Sicardy, B., Braga-Ribas, F., et al. 2023, Nature, 614, 239
Nordgren, T. E., Germain, M. E., Benson, J. A., et al. 1999, AJ, 118, 3032
Ortiz, J. L., Gutiérrez, P. J., Casanova, V., & Sota, A. 2003, A&A, 407, 1149
Ortiz, J. L., Duffard, R., Pinilla-Alonso, N., et al. 2015, A&A, 576, A18
Ortiz, J. L., Santos-Sanz, P., Sicardy, B., et al. 2017, Nature, 550, 219
Ortiz, J. L., Pereira, C. L., Sicardy, B., et al. 2023, A&A, 676, L12
Pereira, C. L., Sicardy, B., Morgado, B. E., et al. 2023, A&A, 673, L4
Pereira, C. L., Braga-Ribas, F., Sicardy, B., et al. 2024, MNRAS, 527, 3624
Pereira, C. L., Braga-Ribas, F., Sicardy, B., et al. 2025, ApJ, 992, L19
Rabinowitz, D. L., Schaefer, B. E., & Tourtellotte, S. W. 2007, AJ, 133, 26
Rizos, Fernández-Valenzuela, E., Ortiz, J. L., et al. 2024, A&A, 689, A82
Rizos, J. L., Ortiz, J. L., Rommel, F. L., et al. 2025, A&A, 697, A62
Rommel, F. L., Braga-Ribas, F., Desmars, J., et al. 2020, A&A, 644, A40
Rommel, F. L., Braga-Ribas, F., Ortiz, J. L., et al. 2023, A&A, 678, A167
Rommel, F. L., Fernández-Valenzuela, E., Proudfoot, B. C. N., et al. 2025a, PSJ, 6, 48
Rommel, F. L., Proudfoot, B. C. N., Holler, B. J., Ortiz, J. L., & Fernández-Valenzuela, E. 2025b, RNAAS, 9, 62
Rousselot, P., & Petit, J. 2010, in AAS/Division for Planetary Sciences Meeting Abstracts, 42, 40.19
Russell, H. N. 1916, ApJ, 43, 173
Santos-Sanz, P., Ortiz, J. L., Sicardy, B., et al. 2020, MNRAS, 501, 6062
Santos-Sanz, P., Gomes-Júnior, A. R., Morgado, B. E., et al. 2025, arXiv e-prints [arXiv:2510.06366]
Sheppard, S. S., & Jewitt, D. C. 2003, Earth Moon Planets, 92, 207
Sicardy, B., Braga-Ribas, F., Buie, M. W., Ortiz, J. L., & Roques, F. 2024, A&A Rev., 32, 6
Sickafoose, A. A., Bosh, A. S., Levine, S. E., et al. 2019, Icarus, 319, 657
Sickafoose, A. A., Bosh, A. S., Emery, J. P., et al. 2020, MNRAS, 491, 3643
Stansberry, J. A., Cruikshank, D. P., Grundy, W. G., et al. 2005, in AAS/Division for Planetary Sciences Meeting Abstracts, 37, 52.05
Stansberry, J., Grundy, W., Brown, M., et al. 2008, in The Solar System Beyond Neptune, eds. M. Barucci, H. Boehnhardt, D. Cruikshank, A. Morbidelli, & R. Dotson (University of Arizona Press), 161
van Belle, G. T. 1999, PASP, 111, 1515
Vara-Lubiano, M., Fernández-Valenzuela, E., Kretlow, M., et al. 2023, in Planetary Sciences and Exploration of the Solar System (7th CPESS), 80575
Verbiscer, A. J., Helfenstein, P., Porter, S. B., et al. 2022, PSJ, 3, 95
White, N. M., & Feierman, B. H. 1987, AJ, 94, 751

[1] Instituto de Astrofísica de Andalucía, IAA-CSIC, Glorieta de la Astronomía s/n, 18008 Granada, Spain
[2] LIRA, CNRS UMR8254, Observatoire de Paris, Meudon, France
[3] Federal University of Technology – Paraná (PPGFA/UTFPR), Curitiba, PR, Brazil
[4] Laboratório Interinstitucional de e-Astronomia (LIneA), Rio de Janeiro, RJ, Brazil
[5] Observatório Nacional (MCTI), Rio de Janeiro, RJ, Brazil
[6] LTE, Observatoire de Paris, Université PSL, Sorbonne Université, Université de Lille, LNE, CNRS, Paris, France
[7] Türkiye National Observatories, TUG, Antalya, Türkiye

[8] The Scientific and Technological Research Council of Türkiye (TÜBİTAK), Ankara, Türkiye
[9] naXys, Department of Mathematics, University of Namur, Namur, Belgium
[10] Federal University of Rio de Janeiro – Observatory of Valongo, Rio de Janeiro, Brazil
[11] Instituto de Física, Universidade Federal de Uberlândia, Uberlândia, MG, Brazil
[12] UNESP – São Paulo State University, Grupo de Dinâmica Orbital e Planetologia, Guaratinguetá, SP, Brazil
[13] Institut Polytechnique des Sciences Avancées (IPSA), Ivry-sur-Seine, France
[14] Deutsches Zentrum für Astrophysik (DZA), Görlitz, Germany
[15] Florida Space Institute, University of Central Florida, Orlando, FL, USA
[16] Department of Space Sciences and Technologies, Akdeniz University, Antalya, Türkiye
[17] Trans-Tasman Occultation Alliance (TTOA), Wellington, New Zealand
[18] Institute of Astronomy and Astrophysics, University of Tübingen, Germany
[19] PADC/DIO, Observatoire de Paris, PSL University, France
[20] Observatoire des Engarouines, Malemort-du-Comtat, France
[21] International Occultation Timing Association (IOTA), Fountain Hills, AZ, USA
[22] Institute for Astronomy, University of Edinburgh, Edinburgh, UK
[23] Société Astronomique de France (SAF), Paris, France
[24] Grupo Alfa Crucis, Brazil
[25] Lowell Observatory, Flagstaff, AZ, USA
[26] Alma Mater Studiorum – University of Bologna, Department of Physics and Astronomy "A. Righi", Bologna, Italy
[27] KinetX, Inc., Space Navigation and Flight Dynamics Practice, Simi Valley, CA, USA
[28] Universidade Estadual de Ponta Grossa (UEPG), Ponta Grossa, Brazil
[29] Sapienza Università di Roma, Rome, Italy
[30] Campo Catino Astronomical Observatory, Guarcino, Italy
[31] INFN, Sezione Roma1, Rome, Italy
[32] INAF OAC, Via della Scienza, Selargius, Italy
[33] Kenyon Astrophysical Observatory (KAO), Northern California, USA
[34] Skynet Robotic Telescope Network, University of North Carolina, Chapel Hill, NC, USA
[35] Johnson Space Center Astronomical Society, Houston, TX, USA
[36] Independent observer, Santana de Parnaíba, SP, Brazil
[37] Independent observer, 77630 Arbonne-la-Forêt, France
[38] Department of Physics and Astronomy, Appalachian State University, Boone, NC, USA
[39] Centro de Amigos de la Astronomia Reconquista – CAAR, Reconquista, Argentina
[40] Rand Observatory II – MPC W71, Lake Placid, NY, USA
[41] Pontificia Universidad Católica de Chile, Center for Astro Engineering, Santiago, Chile
[42] Asociación Argentina Amigos de la Astronomía, Argentina
[43] Cruz del Sur Private Observatory, El Peral, San Juan Province, Argentina
[44] Westport Astronomical Society, Westport, Connecticut, USA
[45] University of New Haven, West Haven, CT, USA
[46] SONEAR Observatory – CEAMIG, Caeté, Minas Gerais, Brazil
[47] Centro de Estudos Astronômicos de Minas Gerais (CEAMIG), Belo Horizonte, Brazil
[48] Space sciences, Technologies & Astrophysics Research (STAR) Institute, University of Liège, Liège, Belgium
[49] Université Côte d'Azur, Observatoire de la Côte d'Azur, CNRS, Laboratoire Lagrange, Nice, France
[50] Complejo Astronómico El Leoncito (CASLEO), San Juan, Argentina
[51] Facultad de Ciencias Astronómicas y Geofísicas (UNLP), La Plata, Argentina
[52] Instituto de Astronomía y Física del Espacio, CONICET–Universidad de Buenos Aires, Argentina
[53] Agrupaciones Astronómicas de Madrid (AAM) y Teruel (ACTUEL), Spain
[54] El Catalejo Observatory (MPC I48), Santa Rosa, La Pampa, Argentina
[55] Los Cabezones Observatory (MPC X12), Santa Rosa, La Pampa, Argentina
[56] Federal University of Espírito Santo: Vitória, Espírito Santo, Brazil

Appendix A: Ingress and egress times from light-curve modelling

Table A.1: Ingress and egress times obtained from the light curve modelling of all positive detections.

Event	Site	Ingress time (UT) (hh:mm:ss.s)	Egress time (UT) (hh:mm:ss.s)	Chord length (km)	Light curve (Fig.)
17 Aug 2020	Lake Placid	01:36:59.90 (0.90)	01:37:38.54 (0.92)	461.59 (15.4)	E.0a
	Naperville	01:38:21.50 (1.10)	01:39:22.24 (1.06)	738.02 (18.3)	E.0b
	Chester	01:38:02.48 (0.10)	01:38:31.71 (0.09)	350.82 (1.6)	E.0c
13 Oct 2020	Running Springs	02:00:21.52 (0.01)	02:01:05.06 (0.39)	687.3 (6.2)	E.0d
	Glendale	02:00:45.99 (0.02)	02:01:29.34 (0.76)	685.3 (12.4)	E.0e
	Lowell Obs. (TiMo)[a]	-	02:01:30.22 (0.02)	-	E.0f
	Tucson	02:00:57.68 (0.12)	02:01:34.16 (0.09)	578.0 (2.3)	E.0g
	Carefree	02:00:47.00 (0.04)	02:01:30.59 (0.01)	689.1 (0.7)	E.0h
	Fountain Hills	02:00:48.66 (0.01)	02:01:31.61 (0.01)	679.1 (0.4)	E.0i
	Scottsdale	02:00:47.33 (0.02)	02:01:31.79 (0.02)	691.6 (0.4)	E.0j
	Tempe	02:00:48.17 (0.03)	02:01:30.69 (0.02)	672.0 (0.5)	E.0k
28 Apr 2021	OPD	07:34:38.43 (0.005)	07:34:56.47 (0.022)	251.1 (0.3)	E.0l
	Reconquista	07:36:21.60 (0.78)	07:37:02.93 (0.81)	575.4 (15.7)	E.0m
	La Canelilla	07:37:44.56 (0.19)	07:38:09.72 (0.19)	350.1 (3.7)	E.0n
	CTIO One-Meter	07:37:49.83 (0.83)	07:38:02.49 (0.32)	176.3 (12.4)	E.0o
	PROMPT-6	07:37:50.05 (0.35)	07:38:02.51 (0.01)	173.5 (4.9)	E.0p
	CASLEO - ASH	07:37:28.12 (1.12)	07:38:15.29 (0.57)	656.4 (17.5)	E.0q
20 May 2021	Bartlett Lake	06:45:14.26 (0.26)	06:45:48.96 (0.13)	726.7 (5.5)	E.0r
	Scottsdale	06:45:14.84 (0.03)	06:45:48.97 (0.03)	715.4 (1.1)	E.0s
	Clear Lake Shores	06:44:19.36 (0.27)	06:44:52.59 (0.21)	699.0 (7.3)	E.0t
	Fountain Hills	06:45:14.85 (0.39)	06:45:48.62 (0.40)	704.6 (11.8)	E.1u
17 Aug 2021	Heaven's Mirror	11:33:12.16 (1.08)	11:34:13.79 (1.06)	769.2 (26.8)	E.1v
2 Jun 2022	Glenlee	18:06:43.11 (0.05)	18:06:47.55 (0.06)	104.3 (2.5)	E.1w
30 Jun 2022	UTFPR	00:25:00.41 (0.84)	00:25:19.50 (1.78)	477.4 (49.2)	E.1x
	UEPG	00:25:01.67 (0.23)	00:25:22.52 (0.24)	532.1 (12.4)	E.1y
	Orion	00:24:48.17 (2.46)	00:25:15.84 (2.63)	736.7 (46.3)	E.1z
	YPO	00:24:44.11 (1.37)	00:25:10.19 (1.47)	655.1 (77.9)	E.1aa
28 Jul 2023	SOAR	06:09:16.73 (0.13)	06:09:45.77 (0.14)	594.1 (4.0)	E.1ab
	CAO	06:09:17.98 (0.03)	06:09:44.95 (0.05)	551.6 (2.5)	E.1ac
	Danish/ESO	06:09:12.23 (0.04)	06:09:45.28 (0.02)	675.9 (0.5)	E.1ad

Notes. The 1σ error bars are in seconds. [a] 5× binned to improve S/N.

Appendix B: Detection limits on additional material around Ixion

We analysed the light curves from all the events studied in this work to search for additional material around Ixion. Following the procedures outlined in Morgado et al. (2023), Pereira et al. (2023), Braga-Ribas et al. (2023), and Pereira et al. (2024), we determined the upper limits for the apparent equivalent width and optical depth obtained from $E'_p = [1 - \phi(i)]\Delta r(i)$ and $\tau = \tau'/2$ (where $\tau' = -\ln(1 - p'_{3\sigma})$), respectively. Table B.1 presents the results obtained in each event. The limits were determined using the original spatial resolution δ_r in the regions external to the occultation by the central body (when a positive detection), covering a certain distance in the sky plane, not necessarily centred on the body's position. Using as an example the light curve obtained at OPD for the 28 April 2021 event, the 3σ limit for the apparent equivalent width is $E'_p = 400$ metres. This indicates that an opaque structure with a width in the sky plane of $W_\perp > 400$ meters would cause a flux drop in the light curve above our 3σ cut. On the other hand, a structure with an apparent width $W_\perp = 2.1$ km (δ_r) would be detected if its optical depth were $\tau > 0.1$. We can compare the detection limits obtained for Ixion with the physical properties of known rings around other small bodies. In our example using the April 2021 light curve from OPD, Chariklo's densest ring (C1R) would be detected (E_p~2 km). Additionally, the Q1R ring around Quaoar and Haumea's ring would also be detected if present around Ixion.

Table B.1: Detection limits on additional material derived from all light curves.

Date	Site	δ_r [km]	E'_p [km]	τ	Sky Cover [km]
2020-08-17	Lake Placid	35.8	29.4	0.5	7 913
2020-08-17	Naperville	59.8	57.3	0.6	12 255
2020-08-17	Chester	3.6	4.4	0.8	1 581
2020-10-13	Running Springs	0.5	0.6	0.7	1 371
2020-10-13	Lowell Observatory (TiMo)	3.9	2.4	0.3	3 648
2020-10-13	Glendale	2.1	1.6	0.4	3 833
2020-10-13	Carefree	0.5	1.0	1.5	2 298
2020-10-13	Scottsdale	0.5	0.6	0.7	4 047
2020-10-13	Fountain Hills	0.5	0.5	0.5	3 798
2020-10-13	Tempe	2.1	1.5	0.4	3 884
2020-10-13	Tucson	1.0	1.5	0.9	5 552
2020-10-13	Clear Lake Shores	5.3	5.9	0.7	14 421
2020-10-13	Gardnerville	5.3	3.9	0.4	2 898
2021-04-28	PROMPT-6	13.9	4.4	0.2	16 330
2021-04-28	CTIO One-meter	13.9	1.4	0.05	16 860
2021-04-28	Observatório do Pico dos Dias	2.1	0.4	0.1	14 801
2021-04-28	La Canelilla	7.0	13.6	1.6	6 699
2021-04-28	Reconquista	69.6	32.6	0.3	26 124
2021-04-28	CASLEO - Cerro Burek ASH	139.2	68.4	0.3	20 835
2021-04-28	A.A.A.A.	69.5	107	1.0	17 936
2021-04-28	Cruz del Sur	83.4	0.4	0.6	4 023
2021-04-28	Trappist-South	34.8	4.3	0.06	15 433
2021-04-28	Observatório Los Cabezones	69.5	54.9	0.5	14 208
2021-04-28	Observatório El Catalejo	27.8	35	0.8	14 183
2021-05-20	Westport Astronomical Society	21.0	42.4	1.7	7 595
2021-05-20	Clear Lake Shores	22.5	30.5	0.9	12 590
2021-05-20	Barltlett Lake Turnoff	22.1	16.0	0.4	4 811
2021-05-20	Scottsdale	33.6	22.9	0.4	5 514
2021-05-20	Fountain Hills	41.9	29.6	0.4	11 330
2021-08-17	Heaven's Mirror	37.4	18.8	0.3	12 994
2022-06-02	Glenlee	7.5	3.9	0.3	5 563
2022-06-30	YPO	50.0	46.2	0.6	9 416
2022-06-30	Orion Observatory	75.1	32.3	0.2	17 290
2022-06-30	UEPG	25.0	21.5	0.5	17 689
2022-06-30	UTFPR-Neoville	97.5	96.6	0.6	14 021
2022-06-30	SONEAR-CEAMIG	50.1	14.0	0.1	14 546
2023-07-28	Danish/ESO	2.0	0.6	0.1	6 136
2023-07-28	SOAR	4.1	1.8	0.08	19 999
2023-07-28	Campocatino Austral Observatory (CAO)	20.4	4.9	0.1	17 570
2023-07-28	CASLEO - Cerro Burek HSH	122.6	20.6	0.09	19 876

Notes. The limits are at the 3σ level.

Appendix C: Summary of the occultation campaigns

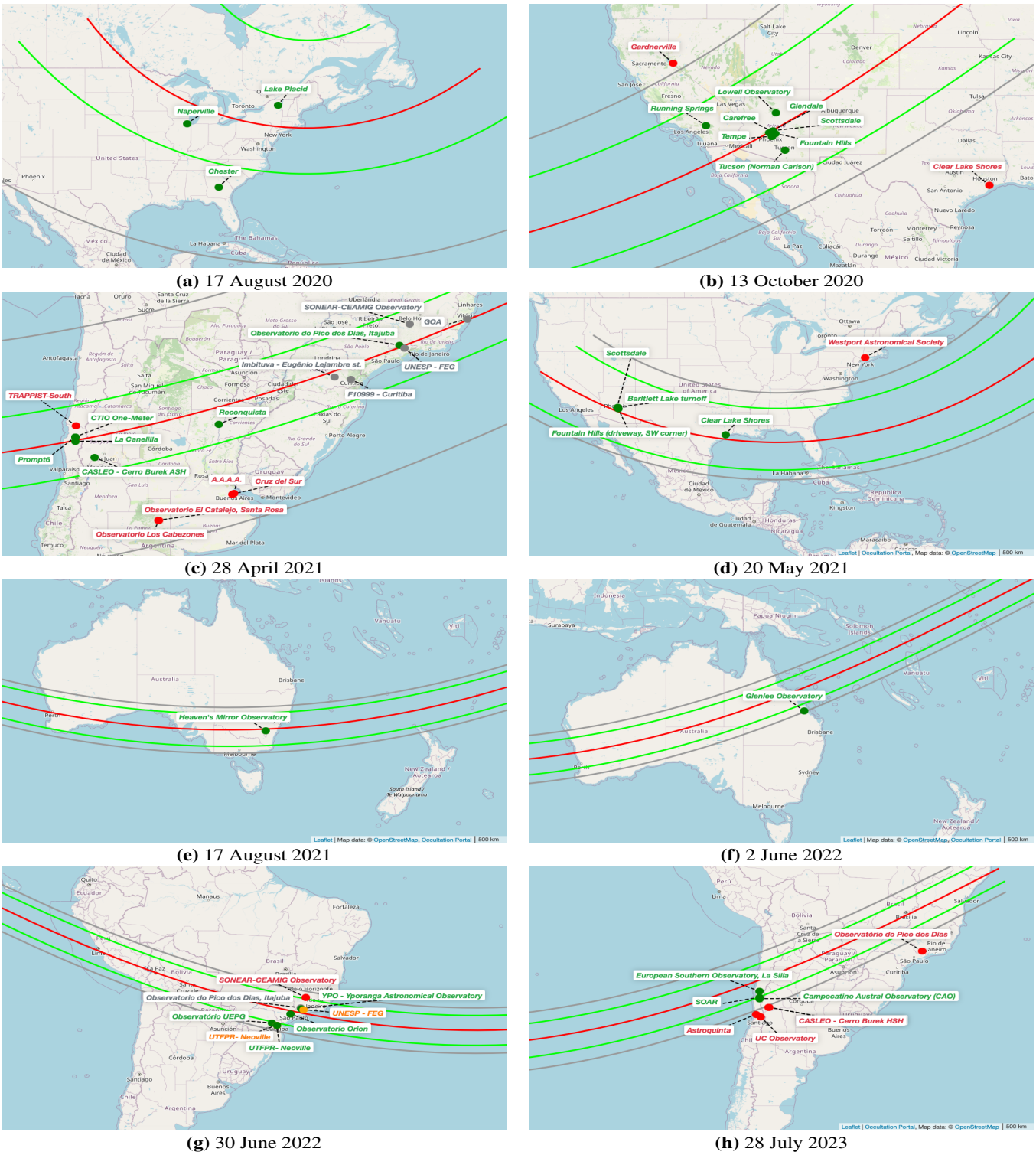

(a) 17 August 2020 **(b)** 13 October 2020

(c) 28 April 2021 **(d)** 20 May 2021

(e) 17 August 2021 **(f)** 2 June 2022

(g) 30 June 2022 **(h)** 28 July 2023

Fig. C.1. Occultation paths for (28978) Ixion events. Each panel corresponds to a specific observation date. Green circles indicate positive detections, red circles negative detections, grey circles overcast conditions, and orange circles technical failures. The green lines show the maximum and minimum shadow diameter limits of Ixion's NIMA prediction, the red line the prediction centre, and the grey band the 1σ uncertainty. Data were compiled via the `Occultation Portal`.

Appendix D: Observation details

The observing circumstances and notation conventions are described in the table footnotes.

Table D.1: Observation details for the occultations by (28978) Ixion.

#	Site (Country) Observer(s)	Latitude (dms) Longitude (dms) Elevation (m)	Transparency Wind Seeing	Telescope (cm) Camera Filter	Method ExpTime TimeSrc	Observation DeadTime
		2020-08-17				
1	Chester (USA) *Roger Venable*	32° 22′ 15.0996″ N 83° 12′ 7.2″ W 104.00	Clear <2 km/h Moderate	T35.6 WAT-910HX Luminance	VID 0.3 s ComNTP	Positive (0 s)
2	Naperville (USA) *Robert Dunford*	41° 45′ 32.4″ N 88° 7′ 0.0084″ W 230.00	Clear <2 km/h Moderate	T35.6 QHY174-GPS Luminance	IMG 5 s CamGPS	Positive (0 s)
3	Lake Placid (USA) *George R. Viscome*	44° 15′ 18.3996″ N 74° 1′ 59.4192″ W 608.00	Clear <2 km/h Good	T30.5 QHY174-GPS Luminance	IMG 3.00088 s CamGPS	Positive (0 s)
		2020-10-13				
1	Lowell Observatory (TiMo) (USA) *Michael Collins*	35° 12′ 10.3644″ N 111° 40′ 1.4628″ W 2198.00	Clear <2 km/h Good	T31.8 Point Grey BFLY Clear	VID 0.050 s ComGPS	Positive (0 s)
2	Scottsdale (USA) *Tony George*	33° 49′ 0.0984″ N 111° 52′ 7.2984″ W 843.00	Clear <2 km/h Moderate	T30.0 Watec 910HX Clear	VID 0.033 s IOTA-VTI	Positive (0 s)
3	Tempe (USA) *Wayne Thomas*	33° 23′ 24.3348″ N 111° 57′ 20.574″ W 358.00	Clear <2 km/h Good	T28.0 RunCam Astro Clear	VID 0.134 s IOTA-VTI	Positive (0 s)
4	Glendale *David A. Kenyon*	33° 41′ 39.0012″ N 112° 12′ 46.0008″ W 400.00	Clear <2 km/h Good	T25.4 RunCam Astro Clear	VID 0.134 s IOTA-VTI	Positive (0 s)
5	Tucson (USA) *Norman Carlson*	32° 18′ 28.314″ N 110° 57′ 46.62″ W 750.00	Clear <2 km/h Moderate	T23.5 RunCam Astro Clear	VID 0.067 s IOTA-VTI	Positive (0 s)
6	Running Springs (USA) *Robert Jones*	34° 13′ 7.8996″ N 117° 7′ 52.3992″ W 1874.00	Clear <2 km/h Good	T20.3 Watec 910HX Clear	VID 0.033 s IOTA-VTI	Positive (0 s)
7	Carefree (USA) *Paul D. Maley*	33° 48′ 42.858″ N 111° 57′ 7.974″ W 654.00	Clear <2 km/h Best	T20.0 Watec 910HX Clear	VID 0.033 s IOTA-VTI	Positive (0 s)
8	Fountain Hills (USA) *Ted Blank*	33° 37′ 21″ N 111° 43′ 35.0004″ W 515.00	Clear <2 km/h Best	T20.0 Watec 910HX Clear	VID 0.033 s IOTA-VTI	Positive (0 s)
9	Gardnerville (USA) *Jerry Bardecker*	38° 53′ 23.4996″ N 119° 40′ 20.3016″ W 1524.00	Clear <2 km/h Good	T30.5 Watec 910HX Clear	VID 0.334 s IOTA-VTI	Negative (0 s)
10	Clear Lake Shores (USA) *Phil C. Stuart*	29° 32′ 55.5101″ N 95° 2′ 6.57996″ W 15.80	Clear <2 km/h Moderate	T20.3 Watec 910BD Clear	VID 0.334 s IOTA-VTI	Negative (0 s)
		2021-04-28				
1	Observatorio do Pico dos Dias (Brazil) Itajuba *G. Rossi, G. Margoti, V. Peixoto*	22° 32′ 7.7532″ S 45° 34′ 57.54″ W 1810.71	Clear <2 km/h Good	T157.4 IXon Clear	IMG 0.15 s CamGPS	Positive (0 s)

Table D.1: Continued.

# Site (Country) 	
Observer(s)
	Latitude (dms)
	Longitude (dms)
	Elevation (m)
		Transparency
		Wind
		Seeing
			Telescope (cm)
			Camera
			Filter
				Method
				ExpTime
				TimeSrc
					Observation
					DeadTime

2 CTIO One-Meter (Chile)	30° 10′ 7.7916″ S	Clear	T100.0	IMG	Positive
	70° 48′ 21.69″ W	<2 km/h	FLI PL23042	1.0 s	(0 s)
J. Pollock, T. Linder	2201.00	Good	Clear	ComNTP	
3 La Canelilla (Chile)	30° 32′ 3″ S	Clear	T52.0	IMG	Positive
	70° 47′ 45″ W	<2 km/h	ZWO1600	0.50112 s	(0 s)
M. Meunier, B. Christophe, L. Bernasconi	1548.00	Good	Clear	ComNTP	
4 CASLEO - Cerro Burek ASH (Argentina)	31° 47′ 13.2″ S	Clear	T45.7	IMG	Positive
	69° 18′ 23.868″ W	<2 km/h	SBIG STL11000	10.0 s	(2 s)
N. Morales, J.L. Ortiz	2591.00	Good	Luminance	ComNTP	
5 PROMPT-6 (Chile)	30° 10′ 3.72″ S	Clear	T40.0	IMG	Positive
	70° 48′ 18.8208″ W	<2 km/h	FLI PL23042	1.0 s	(0 s)
J. Pollock , Vladimir Kouprianov	2166.00	Good	Clear	ComNTP	
6 Reconquista (Argentina)	29° 8′ 25.1826″ S	Clear	T30.5	IMG	Positive
	59° 38′ 36.6086″ W	<2 km/h	QHY174M	5.0 s	(0 s)
Ariel Stechina	50.00	Good	Clear	ComNTP	
7 TRAPPIST-South (Chile)	29° 15′ 16.56″ S	Clear	T60.0	IMG	Negative
	70° 44′ 21.84″ W	20-28 km/h	FLI PL3041-BB	2.5 s	(1.2 s)
Emmanuel Jehin	2315.00	Good	Clear	ComNTP	
8 A.A.A.A. (Argentina)	34° 36′ 18.6984″ S	High humidity	T25.0	IMG	Negative
C.Cebral, M. Konishi	58° 26′ 4.6″ W	<2 km/h	SBIG ST9e	5 s	(0 s)
C. Magliano, Y.O. Cuello	39.40	Good	No filter	Other	
9 Observatorio El Catalejo, Santa Rosa (Argentina)	36° 38′ 15.99″ S	Clear	T20.0	IMG	Negative
	64° 19′ 27.48″ W	<2 km/h	QHY174M GPS	2 s	(0 s)
Julio Spagnotto	182.00	Good	Clear	CamGPS	
10 Observatorio Los Cabezones (Argentina)	36° 38′ 8.28996″ S	Clear	T20.0	IMG	Negative
	64° 17′ 16.8299″ W	<2 km/h	QHY174M-GPS	5 s	(0 s)
A. Wilberger	180.00	Good	Clear	CamGPS	
11 Cruz del Sur (Argentina)	34° 40′ 10.56″ S	Clear	T20.0	IMG	Negative
	58° 34′ 24.276″ W	<2 km/h	QHY174M-GPS	6 s	(0 s)
Andres Chapman	39.00	Bad	Clear	CamGPS	
12 SONEAR-CEAMIG Observatory (Brazil)	20° 42′ 54.27″ S	Overcast	T45.0	IMG	Overcast
	44° 47′ 5.82″ W	-	QHY600	- s	(1.0 s)
C. Jacques	1113.00	-	Clear	ComNTP	
13 UNESP - FEG (Brazil)	22° 48′ 6.0012″ S	Overcast	T40.6	IMG	Overcast
	45° 11′ 25.5984″ W	-	Merlin 247 Raptor	- s	(0 s)
R. Sfair, A. R. Gomes, Jr	540.00	-	Clear	ComGPS	
14 Imbituva - Eugênio Lejambre St. (Brazil)	25° 13′ 39.6527″ S	Overcast	T30.5	IMG	Overcast
	50° 36′ 41.7111″ W	-	Raptor	- s	(0 s)
Chrystian L. Pereira	968.00	-	Clear	CamGPS	
15 GOA (Brazil)	20° 18′ 1.99998″ S	Overcast	T30.4	IMG	Overcast
	40° 19′ 2″ W	-	Canon 600D	- s	(0 s)
M. Malacarne	24.00	-	Clean	ComNTP	
16 F10999 - Curitiba (Brazil)	25° 26′ 10.3926″ S	Overcast	T25.4	IMG	Overcast
	49° 20′ 23.73″ W	-	QHY174M-GPS	- s	(0 s)
F. B. Ribas	1024.00	-	Clear	CamGPS	
	2021-05-20				
1 Fountain Hills (USA)	33° 37′ 27.8868″ N	Clear	T40.6	IMG	Positive
	111° 43′ 39.5879″ W	12-19 km/h	QHY174M-GPS	2.0 s	(0 s)
David W. Dunham, Joan Dunham	518.00	Moderate	Empty	CamGPS	

Table D.2: Continued.

#	Site (Country) Observer(s)	Latitude (dms) Longitude (dms) Elevation (m)	Transparency Wind Seeing	Telescope (cm) Camera Filter	Method ExpTime TimeSrc	Observation DeadTime
2	Scottsdale (USA) AZ *Tony George*	33° 49′ 0.0984″ N 111° 52′ 7.2984″ W 843.00	Clear <2 km/h Moderate	T30.0 WAT910HX Clear	VID 0.533860 s CamGPS	Positive (0 s)
3	Clear Lake Shores (USA) *P. Stuart*	29° 32′ 55.5101″ N 95° 2′ 6.57996″ W 15.80	Clear 2-5 km/h Moderate	T20.3 Watec 910BD EIA None	VID 1.068 s IOTA-VTI	Positive (0 s)
4	Barltlett Lake Turnoff (USA) *Paul D. Maley*	33° 50′ 54.8412″ N 111° 49′ 58.08″ W 996.00	Clear 6-11 km/h Good	T20.0 Watec910HX None	VID 0.0333 s CamGPS	Positive (0 s)
5	Westport Astronomical Society (USA) *Kevin Green, Chang Gao*	41° 10′ 15.8999″ N 73° 19′ 39.2999″ W 88.00	Partly cloudy <2 km/h Good	T35.6 QHY174M-GPS None	IMG 1.00 s CamGPS	Negative (0 s)
	2021-08-17					
1	Heaven's Mirror Observatory (Australia) *W. Hanna*	34° 51′ 50.89″ S 148° 58′ 35.0602″ E 536.00	Clear <2 km/h Moderate	T50.8 QHY174M-GPS None	IMG 3.0 s CamGPS	Positive (0 s)
	2022-06-02					
1	Glenlee Observatory (Australia) *Stephen Kerr*	23° 16′ 10.0597″ S 150° 30′ 1.61841″ E 53.40	Clear <2 km/h Moderate	T30.4 Watec 910BD None	VID 0.32 s IOTA-VTI	Positive (0 s)
	2022-06-30					
1	Observatório UEPG (Brazil) *C. L. Pereira, M. Emilio*	25° 5′ 22.671″ S 50° 5′ 56.7901″ W 923.00	Clear <2 km/h Moderate	T40.6 Raptor Clear	IMG 1.0 s CamGPS	Positive (0 s)
2	Observatorio Orion (Brazil) *Tasso Napoleao, Carlos Colesanti*	23° 34′ 10.2036″ S 47° 12′ 40.5144″ W 884.00	Clear 2-5 km/h Good	T35.6 ATIK One 9.0 No filter	IMG 3.0 s ComNTP	Positive (3.0 s)
3	Yporanga Astronomical (Brazil) Observatory (YPO) *J. Mattei*	22° 41′ 49″ S 45° 31′ 5.99988″ W 1640.00	Clear <2 km/h Good	T14.0 ZWO ASI 6200M LRGB	IMG 2.0 s ComGPS	Positive (1.2 s)
4	UTFPR- Neoville (Brazil) *F. B. Ribas , W. G. Ferrante*	25° 30′ 31.7373″ S 49° 18′ 57.1841″ W 937.67	Clear <2 km/h Good	T11.4 Sony IMX224LQR Clear	IMG 3.971 s ComNTP	Positive (0.016 s)
5	SONEAR-CEAMIG Observatory (Brazil) *C. Jacques*	20° 42′ 54.27″ S 44° 47′ 5.82″ W 1113.00	Clear <2 km/h Good	T45.0 QHY600 Clear	IMG 2 s ComNTP	Negative (1.0 s)
6	Observatorio do Pico dos Dias (Brazil) *J. I. B. Camargo*	22° 32′ 7.7532″ S 45° 34′ 57.54″ W 1810.71	Overcast - -	T160.0 Andor - Ixon Clear	IMG - s CamGPS	Overcast (0 s)
7	UNESP - FEG (Brazil) *G. Rossi, R. Sfair*	22° 48′ 6.0012″ S 45° 11′ 25.5984″ W 540.00	Clear <2 km/h Good	T40.6 Merlin 247 Raptor Clear	IMG - s ComGPS	Technical failure (0 s)
8	UTFPR - Neoville (Brazil) *F. B. Ribas*	25° 30′ 31.7373″ S 49° 18′ 57.1841″ W 937.67	Clear <2 km/h Good	T25.4 QHY174M-GPS Clear	IMG - s CamGPS	Technical failure (0 s)
	2023-07-28					
1	SOAR (Chile) *J. I. B. Camargo, C. L. Pereira*	30° 14′ 16.89″ S 70° 44′ 21.12″ W 2693.95	Clear 2-5 km/h Good	T410.0 Raptor Clear	IMG 0.200 s CamGPS	Positive (0 s)

Table D.3: Continued.

#	Site (Country) Observer(s)	Latitude (dms) Longitude (dms) Elevation (m)	Transparency Wind Seeing	Telescope (cm) Camera Filter	Method ExpTime TimeSrc	Observation DeadTime
2	Danish/ESO (Chile) *C. Snodgrass, M. Bonavita, G. Columba*	29° 15′ 31.7592″ S 70° 44′ 1.464″ W 2345.44	Clear ~20 km/h Good	T154.0 Andor Ixion Ultra red	IMG 0.1 s CamGPS	Positive (0.0 s)
3	Campocatino Austral Observatory (Chile) *A. Zapparata, F. Mallia, G. Isopi*	30° 28′ 15.2905″ S 70° 45′ 53.9015″ W 1525.00	Clear <2 km/h Good	T61.0 Moravian C3-PRO Clear	IMG 1.0 s CamGPS	Positive (0 s)
4	Observatório do Pico dos Dias (Brazil) *L. Liberato, V. Moura* *A.L. Guimaraes, J. Arcas, Silva*	22° 32′ 49.5658″ S 45° 26′ 43.8041″ W 1112.15	Clear 12-19 km/h Moderate	T60.0 Ixon 4269 Empty	IMG 0.2877 s CamGPS	Negative (0.013 s)
5	CASLEO - Cerro Burek HSH (Argentina) *Mario Melita, Luis Mammana*	31° 47′ 13.2″ S 69° 18′ 24.12″ W 2591.00	Partly cloudy 20-28 km/h Moderate	T60.0 SBig Clear	IMG 6.0 s Other	Negative (3 s)
6	UC Observatory (Chile) *N. Castro, L. Vanzi, R. Leiva*	33° 16′ 8.9364″ S 70° 32′ 4.1352″ W 1475.20	Clear <2 km/h Good	T50.0 Raptor Merlin Clear	IMG 5 s ComGPS	Negative (0 s)
7	Astroquinta (Chile) *Leo Peiro*	32° 53′ 0.2796″ S 71° 14′ 55.7412″ W 154.14	Clear <2 km/h Good	T27.9 QHY168C L-eNhance	IMG 10 s ComNTP	Negative (2.7 s)

Site latitude, longitude (format dms) and elevation (AMSL in m) are given in the WGS84 datum. **Telescope**: Tx refers to the telescope aperture in cm. **Method** is the recording method: **IMG** means digital (CCD, CMOS) sequential imaging, while **VID** means analogue video recording. **TimeSrc** refers to the used timing source and method: **GPS**: 1-PPS (one pulse per second) driven video-time-insertion (VID) or camera-internal GPS timestamps (IMG). **NTP**: Network Time Protocol computer system clock synchronisation. **CamGPS**: Camera synchronised directly to a GPS signal for timestamping accuracy. **ComGPS**: Computer synchronised to a GPS signal. **ComNTP**: Computer synchronised using the Network Time Protocol. **TimeBox**: A TimeBox is used for precise time-stamping during observations. **IOTA-VTI**: A hardware device developed by IOTA (International Occultation Timing Association) for video time insertion. **Other**: Any other synchronisation method not listed above. **Transparency** qualitatively describes sky clarity during the observation (e.g. clear, hazy, cloudy, overcast). **Seeing** qualitatively refers to atmospheric stability affecting image sharpness (e.g. good, moderate, poor). Observation can be either positive (occultation detected/recorded) or negative (occultation not detected). **ExpTime** represents the exposure time in seconds, while **DeadTime** refers to the interval between subsequent images in seconds. The sampling cadence is the sum of ExpTime and DeadTime.

Appendix E: Light curves, limb fits, and radial residuals

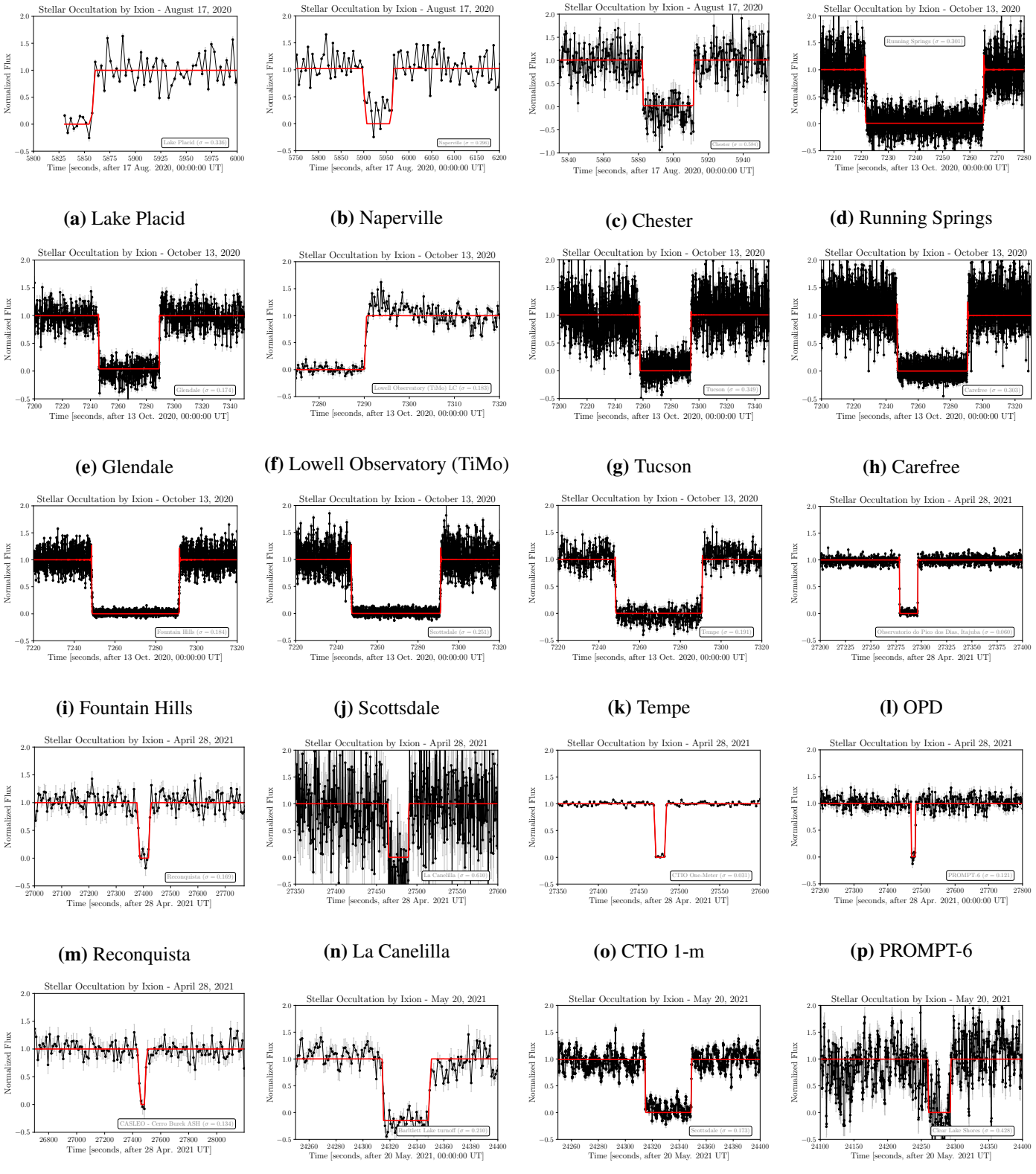

(a) Lake Placid **(b)** Naperville **(c)** Chester **(d)** Running Springs

(e) Glendale **(f)** Lowell Observatory (TiMo) **(g)** Tucson **(h)** Carefree

(i) Fountain Hills **(j)** Scottsdale **(k)** Tempe **(l)** OPD

(m) Reconquista **(n)** La Canelilla **(o)** CTIO 1-m **(p)** PROMPT-6

(q) CASLEO – Cerro Burek ASH **(r)** Bartlett Lake Turnoff **(s)** Scottsdale **(t)** Clear Lake Shores

Fig. E.0. Normalised flux light curves of the stellar occultations by (28978) Ixion. The black points represent the observed flux with uncertainties, and the red line shows the best-fit model. The x-axis represents the time in seconds relative to 00:00:00 UT on the observation date, and the y-axis shows the normalised flux.

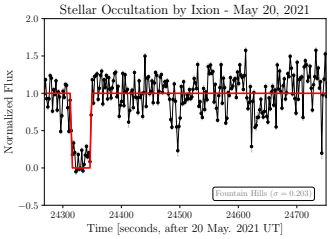

(u) Fountain Hills

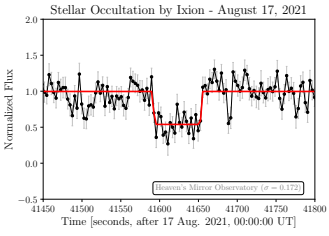

(v) Heaven's Mirror Obs.

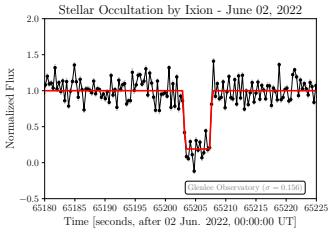

(w) Glenlee Observatory

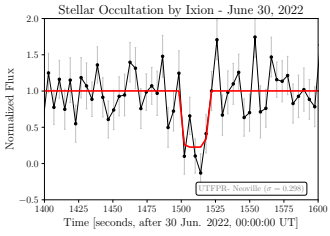

(x) UTFPR–Neoville

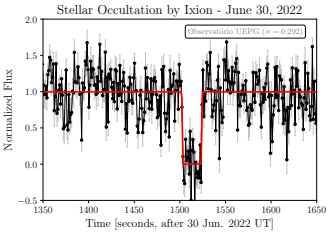

(y) Observatório UEPG

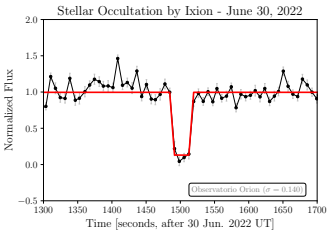

(z) Observatorio Orion

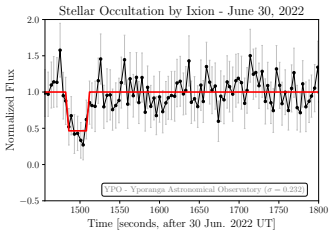

(aa) YPO

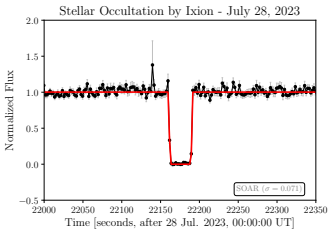

(ab) SOAR

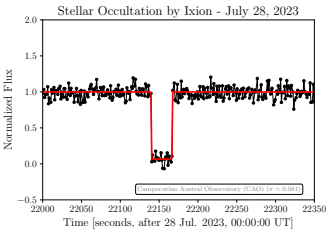

(ac) CAO

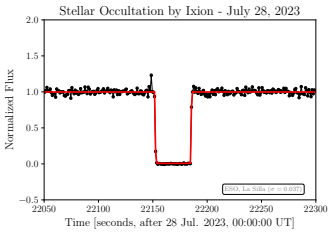

(ad) Danish/ESO

Fig. E.1. Continued.

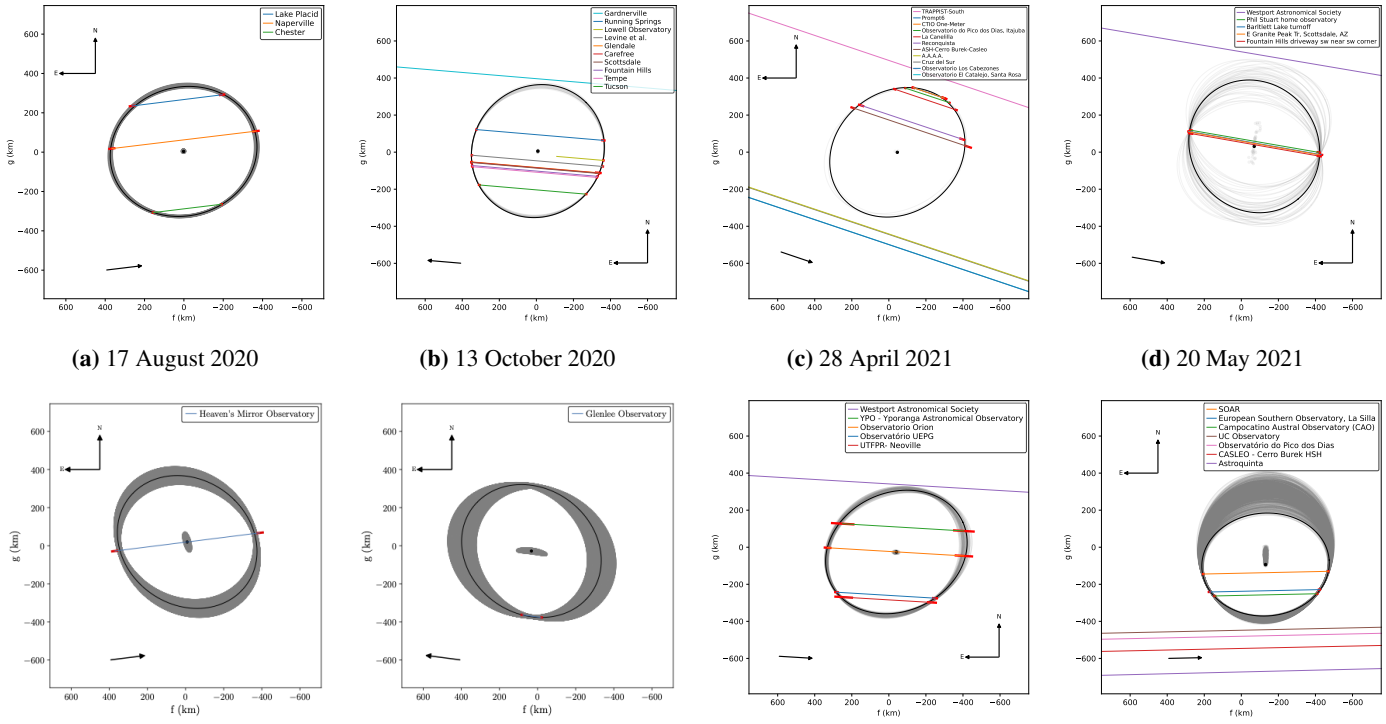

(a) 17 August 2020 **(b)** 13 October 2020 **(c)** 28 April 2021 **(d)** 20 May 2021

(e) 17 August 2021 **(f)** 2 June 2022 **(g)** 30 June 2022 **(h)** 28 July 2023

Fig. E.2. Limb-fit diagrams for the eight stellar occultations by (28978) Ixion: (a) 17 August 2020, (b) 13 October 2020, (c) 28 April 2021, (d) 20 May 2021, (e) 17 August 2021, (f) 2 June 2022, (g) 30 June 2022, and (h) 28 July 2023. Each chord is shown in a different colour, corresponding to the observing sites listed in the legends. Positive detections define the limb of the body, while continuous full-length chords represent negative observations that constrain the maximum extent of the limb. The x- and y-axes correspond to the sky-plane coordinates f and g (in km), oriented along the fundamental plane of the occultation. For the single-chord events (e and f), the limb shape was fixed to the global solution; only the astrometric offsets (f, g) were determined. The red segments at the ends of the chords represent the ingress and egress timing uncertainties. An elliptical fit was applied in each case, with the best-fit solution (1σ) shown. The grey-shaded regions around the ellipses indicate the 1σ confidence domains obtained from the fitting procedure. The corresponding parameters are listed in Table 4. The black arrow indicates the direction of the shadow motion, while the arrows labelled N and S denote celestial north and south, respectively.

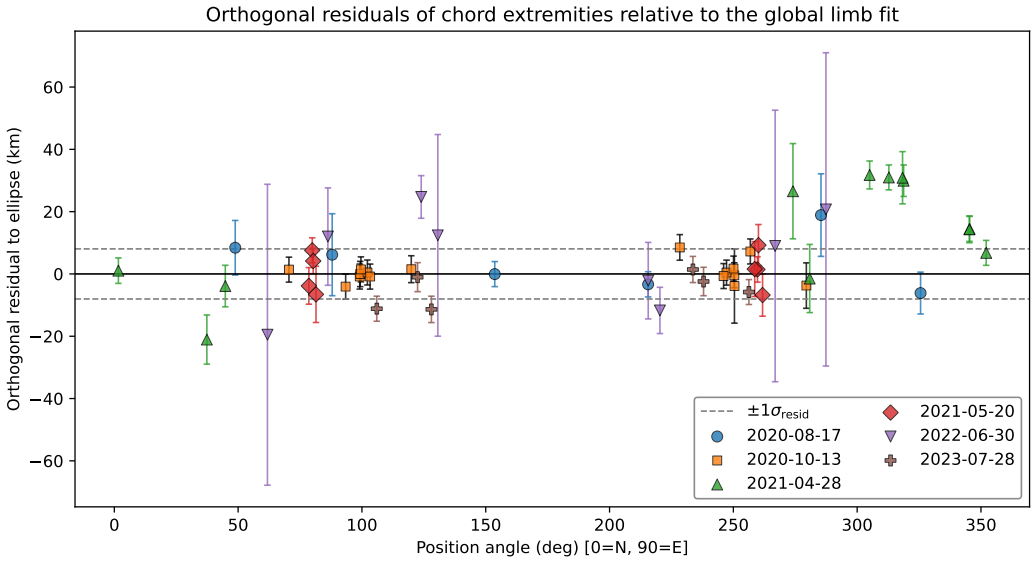

Fig. E.3. Orthogonal (normal) residuals of the chord extremities with respect to the global limb solution, plotted as a function of position angle in the ellipse-aligned frame. Residuals are measured along the local normal to the best-fitting ellipse, ensuring a geometrically consistent assessment of deviations over the entire limb. Each colour and marker corresponds to a different occultation epoch (same coding as in Fig. 2). No clear systematic trend with position angle is observed, indicating that the residuals are consistent with random scatter within the adopted observational and model uncertainties. The offsets observed for the 28 April 2021 and 30 June 2022 epochs are discussed in Sect. 5 and may be associated with changes in the projected figure of the body at different rotational phases or aspect angles.